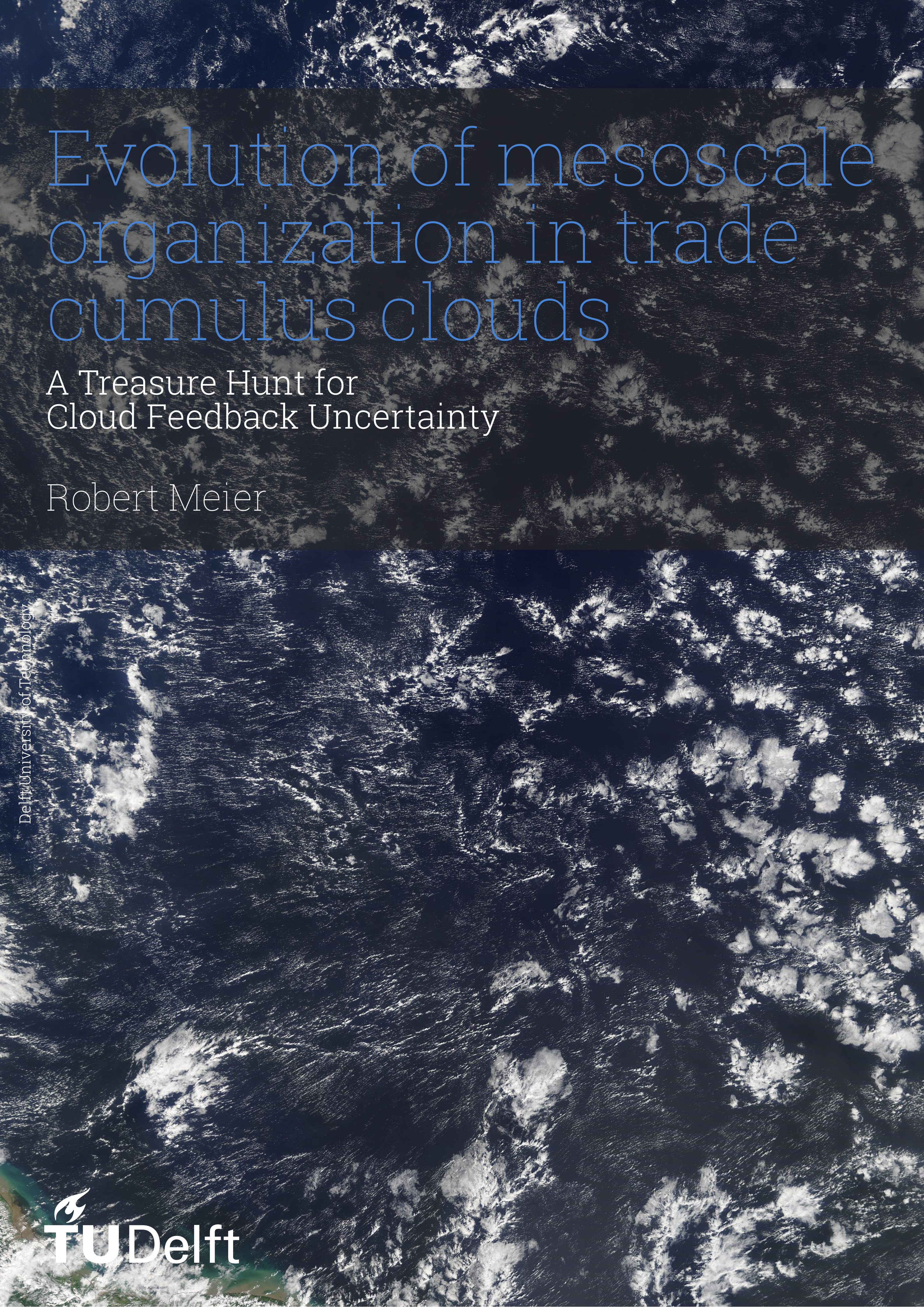

Evolution of mesoscale organization in trade cumulus clouds

A Treasure Hunt for Cloud Feedback Uncertainty

Robert Meier

Delft University of Technology

Evolution of mesoscale organization in trade cumulus clouds

A Treasure Hunt for Cloud Feedback Uncertainty

by

Robert Meier

to obtain the degree of Master of Science
at the Delft University of Technology,
to be defended publicly on Thursday June 13, 2024 at 14:30.

Student number:	not public	
Project duration:	October 9, 2023 – May 30, 2024	
Thesis committee:	Prof. dr. A. P. Siebesma,	TU Delft, supervisor
	Dr. F. Glassmeier,	TU Delft
	Dr. L. Laan,	TU Delft

Cover:	"True Color" image taken by MODIS instrument aboard the Aqua and Terra satellite on January 8 2020, retrieved from NASA Worldview
Style:	TU Delft Report Style, with modifications by Daan Zwaneveld

An electronic version of this thesis is available at `http://repository.tudelft.nl/`.

Preface

My personal journey to this thesis in atmospheric science was not particularly straightforward, but all the more exciting. Starting with my bachelor's degree in physics out of admiration for the stars and the universe, I was soon drawn into solid state physics. My enthusiasm for renewable energies brought me to Delft for an exchange year, where I finally became so fascinated by clouds that I did not want to leave anymore.

Since I first learned of the greenhouse effect, I have always been curious to understand more about our planet and its climate. This curiosity got refreshed during the atmospheric physics course taught by Stephan de Roode and my supervisor, Pier Siebesma. By their inspiring enthousiasm I got convinced that without a lot of prior knowledge about the atmosphere and remote sensing I want to learn more about the mysterious patterns in clouds and their effect on the climate. Certainly this project would not have been possible alone and I want to express my gratitude to the ones that supported me in the process.

First, I want to thank Pier not only for giving the inspiring course at the physics faculty, but also for supervising this project and sharing his deep understanding of shallow cumulus and both his hope and skepticism about mesoscale signals. Knowing of his full schedule, I appreciated every moment of discussion we had.

A warm thank you goes to Franziska Glassmeier for her boundless enthusiasm for cloud patterns and her stimulating vision of a conceptual landscape of (meta)stable mesoscale states. Even during her stay in the USA she did not miss out on our weekly discussions about the search for the mesoscale. Her detailed feedback, both in terms of content and language, was extremely helpful. I am very grateful having been invited for many cloud organization meetings and I enjoyed our discussions from timescale separation and quasipotentials to how to save the climate.

Further, I would like to thank Liedewij Laan for joining my assessment committee and for attending my intermediate evaluation without having much background on clouds, but being enthousiastic about the project and making me reflect on interesting questions about the methodology.

A deep thanks goes to Pouriya Alinaghi. Although not being an official member of the assessment committee, he always took the time to discuss problems in person or have a quick coding session and he accelerated my progress by his many great ideas on how to analyze the data. I am very grateful to him for sharing his optimism about my results, convincing me of their significance for the scientific community and for motivating me to find my own style in writing without too much hesitation. I loved to watch his simulations on cold pools and see his sharp sense of details. Together with Franziska, he helped making this thesis more clear and concise.

Many thanks go to Ryan Eastman, Geet George and Martin Janssens. To Ryan for providing the trajectories that made this study possible first of all. His experience in the field has been incredibly valuable and I really appreciated the meetings with him and his feedback on the results. To Geet for his expertise on satellite data processing and for sharing his code on accessing GOES-16 data. He was extremely helpful with running scripts on the VRLab cluster and together with Nina Robbins he made the satellite images more easily accessible for me. And to Martin, whose cloud metrics paper shaped the way I think about mesoscale patterns and who showed big interest in my project from the start on. His technical help with the cloudmetrics python package was very appreciated.

Finally, my heartfelt gratitude to my parents, who supported me throughout my entire studies and who I visit far too rarely. Thanks to my friends from the Applied Physics Master for welcoming me as an exchange student, teaching me the Dutch language and traditions and for making my first year in Delft unforgettable. At last, I want to thank the person who gave me another good reason to stay in Delft. Thank you, Fenna, for always being there for me and cleaning up the mess in my head from time to time, especially during challenging periods like the writing of this thesis.

Robert Meier
Delft, June 2024

Summary

How clouds change due to global warming is a major source of uncertainty in global climate models. A large part of this uncertainty originates from the feedback of low clouds over the subtropical ocean. The processes that shape these clouds range from microphysical processes of condensation and evaporation to the large-scale circulations spanning thousands of kilometers. While different models can resolve the large scale circulations and the small scale of individual clouds increasingly well, there is a gap in understanding the scale in between: the mesoscale with its fascinating patterns. They exhibit a large continuous variability that affects not only their visual appearance, but also the amount of sunlight they reflect.

This thesis aims to analyze the temporal evolution of the mesoscale cloudiness by following the clouds on their path over the Atlantic along the trade winds and characterize their patterns by cloud metrics, cloud cover and mean cloud object length, computed on geostationary satellite images. Both decrease as the cloud fields move over warmer waters. The most prominent feature is the diurnal cycle in the cloud metrics that can at least partially be explained by oscillations in the atmospheric stability and the surface wind speed of the large-scale environment. Following the line of evidence found from these cloud controlling factors, we conclude that the decrease in low cloud amount and size due to increase in sea-surface temperature will most likely overcompensate the rise in cloud object size due to increase of stability. Especially stratocumulus clouds might become much less and also smaller. However, there remains a large, seemingly random variability in the cloud metrics that has little mean contribution to the climatology. As we cannot expect this to be the case in a warmer climate, we still need to understand what causes this variability. Therefore, the trade wind cloudiness needs to be further investigated with higher temporal resolution of the cloud controlling factors, more trajectories to bin for a fixed large-scale and better understanding of the interplay of governing processes both from models and observations.

Contents

1

Introduction

The climate on Earth is strongly influenced by the presence of clouds. Clouds affect our planets energy budget by reflecting shortwave solar radiation back into space and by absorbing longwave (infrared) radiation from the surface and thereby contributing to the greenhouse effect. The net cloud radiative effect (CRE) is the difference in outgoing short- and longwave radiation between the so called all-sky (with clouds) and a potential clear-sky. Overall, the clouds longwave warming effect of $28\,\mathrm{W/m^2}$ is compensated by their shortwave cooling effect of $47\,\mathrm{W/m^2}$, which results in a net cooling effect of $19\,\mathrm{W/m^2}$ (Forster et al., 2021). Clouds at higher altitudes have a stronger warming effect and clouds with a higher albedo are cooling more as they reflect more sunlight. In a changing climate the altitude, albedo and the amount of clouds are altered, causing a change in CRE, which leads to one of the most important feedback mechanisms in the climate system. While the confidence increases that cloud feedback is positive, the results from different global climate models (GCMs) still range from a slightly negative feedback to one of the strongest positive feedbacks. This uncertainty propagates into the equilibrium climate sensitivity which characterizes the increase in global surface temperature for a doubling in CO_2 concentration, which has a very likely range of 2–5 K with 3 K as a central value (cf. Tab. 7.13 in Forster et al. (2021). Though mitigation of climate change remains crucial in all scenarios, a more accurate projection of climate change is essential for the development of adaptation plans, that may take decades to implement. Thus, a reduction in the uncertainty of the cloud feedback is one big step towards this goal.

Depending on the location on the planet, clouds can exhibit various types (cf. Figure 1.1). In the intertropical convergence zone (ITCZ) the moist air above the warm pools forms deep convective towers that reach up to the tropopause, where the air masses flow polewards. Over the colder subtropical ocean the air masses subside again, thereby lowering the inversion, which leads to shallower convection like stratocumulus and shallow cumulus. This large-scale circulation, named after its discoverer George Hadley and spanning between the equator and 30°N/S, is closed by the trade winds. Their movement towards the equator is deflected to the west by the Coriolis force, leading to north-easterly trade winds on the northern hemisphere.

Over the last decades an advance in understanding the global cloud feedback came from studying different cloud regimes and their main underlying processes separately (Gettelman et al., 2016). The feedback of marine boundary layer clouds has been the one with the largest uncertainty and was the main cause of the large inter-model spread in estimates on climate sensitivity (Bony, 2005; Vial, Dufresne, et al., 2013). The sub-regimes of stratocumulus, located at the eastern edge of the subtropical oceans, and shallow cumulus together cover 29 % of Earth's surface between 60°N/S with the largest fraction over the (sub-)tropical ocean (Scott et al., 2020). The stratocumulus regime is characterized by strong subsidence and large tropospheric stability. The large cloud decks transition along the trade winds into the shallow cumulus

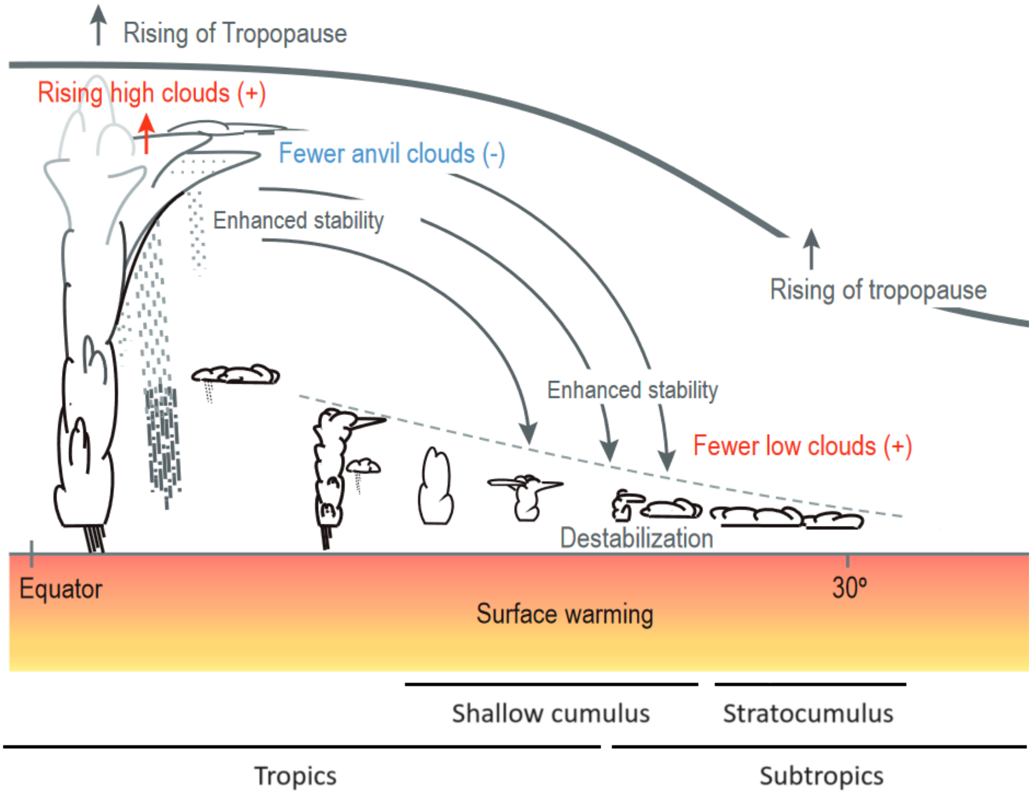

Figure 1.1: Schematic cross section of diverse cloud responses to surface warming from the tropics to polar regions. Thick solid and dashed curves indicate the tropopause and the subtropical inversion layer in the current climate, respectively. Thin grey text and arrows represent robust responses in the thermodynamic structure to greenhouse warming, of relevance to cloud changes. Text and arrows in red, orange and green show the major cloud responses and their sign assessed with high, medium and low confidence, respectively. Adapted from Fig. 7.9 from Forster et al. (2021).

regime (Sandu et al., 2010), which we therefore also refer to as trade cumulus. Their regime is characterized by weaker subsidence and a smaller tropospheric stability, but also an increased sea-surface temperature as the clouds move towards the equator. While stratocumulus have a larger cloud cover than trade cumulus, the regime of trade cumulus is far larger (Medeiros and Stevens, 2009), making both regimes and the transition from one to the other very important for global cloud feedback estimates. As low clouds, they are both known to have a strong negative effect onto the planets energy budget (Hartmann et al., 1992). On the other hand, they are likely to have the strongest positive feedback of all cloud regimes and after tropical high clouds the one with the largest uncertainty (Forster et al., 2021; Sherwood et al., 2020).

Ten years ago, Stevens and Bony (2013) stated that the GCMs cannot resolve processes that couple cloud formation, moist convection and heating to the large-scale circulation. The marine boundary-layer clouds are especially dependent on these unresolved processes and shallow cumuli are not well represented by their parameterized versions in GCMs (Konsta et al., 2022). The community reacted with two different lines of evidence to better resolve the cloudiness in the trades. In order to understand the coupling of clouds to the large-scale circulation, "cloud controlling factors" (CCFs) were defined, like sea-surface temperature SST, estimated inversion strength EIS, surface wind speed and free tropospheric vertical velocity (D. T. McCoy et al., 2017; Myers and Norris, 2016; Qu et al., 2015). The tropical low cloud cover was found to be sensitive to the temporal variability of these large-scale parameters, with a cloud cover reduction due to an increasing SST, while a stronger inversion leads to a higher cloud cover (Qu et al., 2015). Consequently, future cloudiness can be constrained by CCFs that are easier to predict from GCMs, under the assumption that the relationship between cloudiness and CCFs is timescale invariant, i.e. the relationship derived from short timescale data holds true for climatological timescales, and the CCFs fully control cloudiness. For these assumptions Klein et al. (2017) found a contribution of low clouds to the global mean cloud feedback of $(0.25 \pm 0.18)\,\mathrm{W/(m^2\,K)}$ (90 % confidence). As the total feedback is positive this indicates that the cloud cover reduction due to SST increase overrules the increased cloudiness due to the stronger inversion.

The second line of evidence uses high resolution Large-Eddy Simulations (LESs) to resolve turbulent processes in the boundary layer that affect cloudiness in the trades, while the large-scale circulation is parameterized. The resulting cloud feedback summarized by Bretherton (2015) is in line with the feedback found from the CCF analysis.

If the CCF analysis is divided into stratocumulus and trade cumulus regimes, the reduction in low clouds cover is found to be stronger for stratocumulus than for trade cumulus, independent of GCM or observation (Cesana et al., 2019). Radtke et al. (2021) concluded from LES modelling of a trade cumulus cloud field that the cloud feedback of trade cumulus is close to zero. However, both the CCF analysis and the LES models have their shortcomings as they mainly represent one out of three scale ranges that influence trade cumulus clouds: the large-scale environment is well represented by GCMs, the scale of individual clouds is well represented by LES, but the mesoscale is not ideally resolved in both (Janssens, 2023).

This raised the question where to look for the unexplained variance in the regressions from CCFs onto CRE (Scott et al., 2020). The long forgotten mesoscale, that roughly ranges between 20–2000 km depending on the definition, posed a promising objective for further investigations. The spatial organization of stratocumulus clouds due to mesoscale cellular convection has already been studied for much longer (Krueger et al., 1961). For trade cumulus the community mainly focused on the North Atlantic trades east of Barbados, where the EUREC4A field campain (Bony, Stevens, et al., 2017) gave observational insights and the region is known to be representative for other trade cumulus regimes on the planet (Medeiros and Nuijens, 2016). During boreal winter the regime's large-scale conditions are the most undisturbed because the ITCZ is the further south.

Motivated by the effect of mesoscale organization on the CRE of deep convective clouds (Tobin et al., 2012), Stevens, Bony, et al. (2019) was the first to systematically classify mesoscale cloud patterns in the trades from satellite images. Four patterns were classified as robustly identifiable and named after their appearance: Sugar, Gravel, Fish and Flowers. Further, Nuijens et al. (2019) proposed the mesoscale organization of trade cumulus clouds as one of three fields that require deeper understanding to reduce low-cloud feedback uncertainties.

While the first classification process was still based on subjective labelling of cloud field images, there were also first attempts to characterize patterns more objectively. Janssens et al. (2021) described the organization of cloud fields by human-defined metrics frequently used in literature and showed that observed patterns are distributed unimodal and continuously in the metric space. A subset of these metrics was used by Bony, Schulz, et al. (2020) to classify the patterns objectively and correlate their occurrence with CCFs like wind speed and inversion strength. Another approach to characterize the cloud patterns is to use machine learning (Denby, 2020). Both, the classifications by cloud metrics and machine learning were used by Vial, Vogel, et al. (2021) to study the diurnal cycle of pattern occurrence and their cloud cover and of corresponding CCFs. So far only Eulerian snapshots of cloud fields were studied. However, if we want to understand how the underlying processes change the cloud fields over time and how they transition from one organizational pattern to another we need to follow them along the trade winds.

Recently, transitions between closed and open cells in stratocumulus were observed by Eastman, I. L. McCoy, et al. (2022) with a Lagrangian framework that was based on cloud field back

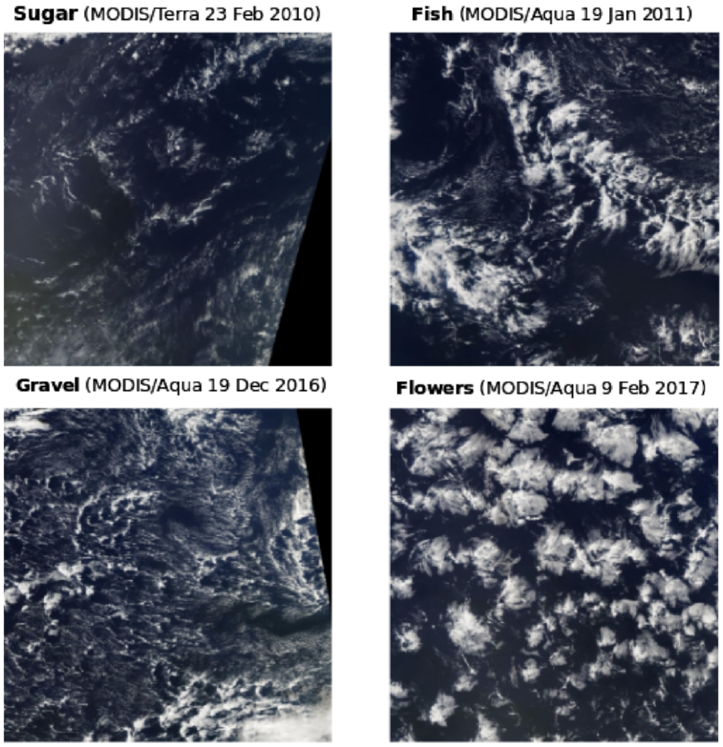

Figure 1.2: Illustration of the four cloud patterns of trade cumulus pointed out by Stevens, Bony, et al. (2019). The four satellite images (48-58°W, 10-20°N) are derived from MODIS imagery. Reprint from Fig.1 a) in Bony, Schulz, et al. (2020).

trajectories for 72 h and MODerate-resolution Imaging Spectroradiometer (MODIS) satellite imagery with a temporal resolution of 12 h. A comparable study for the transition from stratocumulus to trade cumulus was performed by Sandu et al. (2010) and showed that it is controlled by the change in SST and LTS. An investigation of transitions between organizational states of trade cumulus cloud fields is still missing also due to the fact that those transitions happen on shorter timescales. Thanks to the Geostationary Operational Environmental Satellite GOES-16, images every 10 min are available and the possibility to resolve the evolution of trade cumulus cloud fields might be given now.

The scope of this thesis is to give an answer on how the mesoscale organization of trade cumulus cloud fields evolves on timescales of hours up to a week along the trades. We use a Lagrangian framework to follow the trajectories of cloud fields inferred from ERA5 wind fields and compute a subset of cloud metrics from Janssens et al. (2021) on 5°×5° frames of brightness temperature fields obtained every 10 min from GOES-16 for the period of January 1 to February 28, 2020. Further, the cloud metrics are related to CCFs and the remaining unexplained variance is analyzed on possible mesoscale self-organization. More details on the methodology can be found in chapter 2. The results are presented in chapter 3 and further implications as well as possible solutions to limitations in our analysis are discussed in chapter 4. Finally, the conclusions are summarized in chapter 5 and an outlook for future studies is given.
Understanding mesoscale processes dependent and independent of the large-scale might close the gap between the coarse GCMs and the high resolution LES and narrow down the uncertainty in low cloud feedback in a warmer climate.

2

Research design and methods

In this chapter we first introduce what data was used in our analysis, how the trajectories for the Lagrangian framework were built and how we identified low clouds from satellite images. In section 2.4 we discuss and finally chose appropriate thresholds for high cirrus clouds, before we describe the cloud metrics computation and discuss the subset of metrics we chose. Further, our methods used for temporal and ensemble averaging, curve fitting and the computation of the flow fields that show mean tendencies in the cloud metric space are explained. Finally, we shortly introduce multilinear regressions and how they were used to remove large-scale influence from our time series.

2.1. ERA5 trajectories

The trajectories analyzed in this thesis were obtained by Ryan Eastman using the latest reanalysis of the European Centre for Medium-Range Weather Forecast (ECMWF), also called ERA5 (Hersbach et al., 2020). An atmospheric reanalysis assimilates both observational weather data and forecast model output, which is initialized with the observational data. It also takes the uncertainties in the observations and the model output into account and therefore provides a stable analysis of weather data on smaller spatial or temporal grids than actually measured in the past. ERA5 has a spatial resolution of 31 km and a temporal resolution of 1 h with a 3-hourly ensemble uncertainty.

From this dataset the wind fields at 925 hPa were 3D-interpolated in latitude, longitude and time and the corresponding values at planes of constant local hour were used to propagate the trajectory points back and forth in time in steps of six local hours, matching with the pass over times of polar orbiters. The trajectories were initiated on a grid of 2° lat/lon spacing in the central Atlantic trades (12°-22°N and 38°-58°W) at 01:30 local time at every day between January 01 and February 28, 2020. This produced a total of 3894 trajectories with a length of 6 days in local time. As most trajectories move west in the trades, they are longer than 6 days in UTC time. The trajectory points were spline-interpolated from 6-hourly spacing to hourly spacing in local time. Based on this dataset we interpolated the trajectory points again, this time linearly, onto the exact UTC times of the GOES-16 satellite images every 10 min. Along the trajectories the following ERA5 parameters were also 3D-interpolated and obtained every three hours local time by Ryan Eastman:

- sea-surface temperature (SST)
- specific humidity at 700 hPa (q_{700})
- lower troposheric stability (LTS)
- wind speed at 10 m (wsp_{10})

- subsidence at 700 hPa (ω_{700})
- relative humidity at 1000 hPa (RH_{1000})

The first five are frequently used cloud controlling factors (CCFs). The surface relative humidity is replaced in most studies by the free-tropospheric humidity at 700 hPa ((Scott et al., 2020)). Nevertheless, we will also analyze the covariance of the surface relative humidity with the cloud metrics later on and evaluate whether it can control cloudiness.

The large-scale parameters and the 925 hPa wind fields were averaged on circles of 100 km radius around the current lat/lon position of the trajectory, which includes on average 33 ERA5 data points.

The pressure levels p of the given ERA5 parameters can be related to altitudes via the barometric formula

$$z = \frac{T_{\mathrm{ref}}}{\Gamma_{\mathrm{env}}}\left(1 - \left(\frac{p}{p_{\mathrm{ref}}}\right)^{\frac{R\Gamma_{\mathrm{env}}}{Mg}}\right) + z_0 \tag{2.1}$$

with the reference pressure and temperature p_{ref} and T_{ref}, respectively, the altitude of this reference z_0, the environmental lapse rate $\Gamma_{\mathrm{env}} = 6.5\,\mathrm{K/km}$, the universal gas constant R, dry air molar mass M and standard gravity g. By using the ERA5 monthly mean temperature at 1000 hPa for January and February 2020 as a reference the altitudes were computed as shown in Table 2.1. Note that the computed altitudes are strongly dependent on the pressure we assume at sea level, which in reality of course also varies spatially. The used 925 hPa level for measuring the advection of clouds is reasonable when compared to measurements of cloud base height and shallow cloud top heights (Albright et al., 2023).

Table 2.1: Estimates of corresponding altitudes for given pressure levels following the barometric formula and the environmental lapse rate of 6.5 K/km.

pressure level	altitude
1000 hPa	$z_0 = (113 \pm 2)\,\mathrm{m}$
925 hPa	$(780 \pm 12)\,\mathrm{m}$
700 hPa	$(3082 \pm 49)\,\mathrm{m}$

As we want to study the evolution of mesoscale organization above the Atlantic ocean and not above the land, the trajectories were cropped at 58°W and on a linear slope in front of South America. The region that the trajectories were reduced to is shown in Figure 2.1. From the 3894 trajectories, 931 (24 %) show clockwise loops, indicating a proximity to a high pressure field, and 65 (2 %) exhibit counterclockwise loops probably caused by low pressure fields. From the 2898 loop-free trajectories, 2794 are headed westward as expected in the trades. For the further analysis we consider only those loop-free trajectories that move westerly. We can further identify two interesting subgroups inside this set of trajectories. Trajectories that are originated in the northwestern Atlantic (140 trajectories, cf. Figure 2.2a) and trajectories that are originated in the eastern Atlantic close the African continent (1297 trajectories, cf. subset in Figure 2.2b). The remaining trajectories cannot be sorted into one of these groups without doubt, but they are considered in the main analysis of the full set of trajectories.

2.2. Satellite Data

The Geostationary Operational Environmental Satellite 16 (GOES-16, also GOES East) is part of the latest generation of geostationary satellites by NOAA[1] and NASA[2]. Its orbit is at a height of 35 786 km above the nadir at 0°N 75.2°W. The Advanced Baseline Imager (ABI) is a 16-channel passive imaging radiometer onboard of GOES-16 and the primary instrument for observing

---

[1] National Oceanic and Atmospheric Administration

[2] National Aeronautics and Space Administration

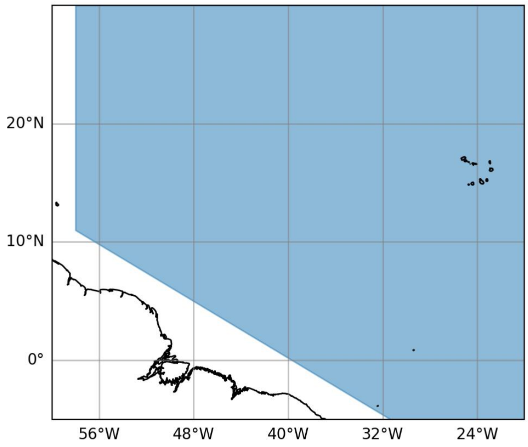

Figure 2.1: Map of the studied domain with the region the trajectories were reduced to (Atlantic ocean) shown in blue.

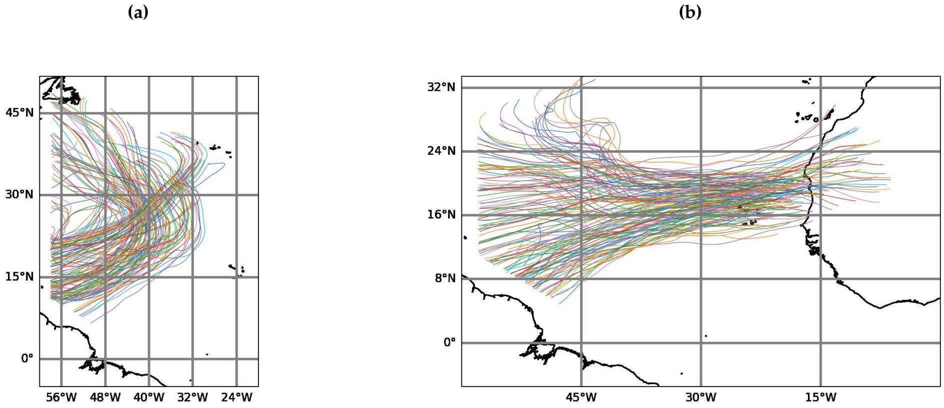

Figure 2.2: Trajectories originated in the northwestern (a) and eastern (b) Atlantic.

the weather, oceans and environment of almost the entire western hemisphere. For weather monitoring the full disk version of the Cloud and Moisture Imagery Product (CMIP) is used, which provides the brightness temperature T_B that relates to the spectral radiance L_λ as

$$L_\lambda = 2hc^2\tilde{\nu}^3 \left[\exp\left(\frac{hc\tilde{\nu}}{k_B(bc1 + bc2 \cdot T_B)}\right) - 1\right]^{-1} \tag{2.2}$$

with h the Planck constant, c the speed of light, k_B Boltzmanns constant and $\tilde{\nu}$ the bands central wavenumber. We recognize Planck's law in this with the temperature

$$T = bc1 + bc2 \cdot T_B \tag{2.3}$$

and band corrections $bc1$ and $bc2$. All 16 ABI-channels from visible to infrared are available in the CMI data product, but for the observation of low clouds channel 13 with a center wavelength of 10.33 µm is most suitable, as low clouds emit radiation with energy densities at its maximum around this wavelength. The band corrections for this channel are $bc1 = 0.0755\,\mathrm{K}$ and $bc2 = 0.999\,75$. Thus, in the range of low clouds, the difference between the cloud top temperature T and T_B is negligible and we can assume

$$T \approx T_B. \tag{2.4}$$

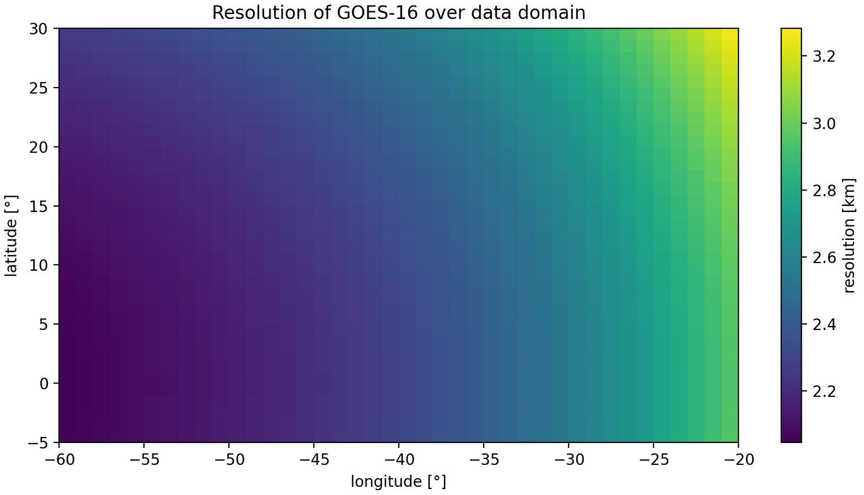

Figure 2.3: Effective resolution of GOES-16 images over the observed domain. The further away from the nadir at 0°N 75.2°W the more the altitude angle of the satellite varies from 90° and the lower the resolution effectively.

Together with the environmental temperature lapse rate this gives an indication for the cloud top height, which makes it possible to classify low clouds (c.f. section 2.3).

The satellite data is localized on the ABI fixed grid with the scanning angles x and y as coordinates. These coordinates can be translated to geographic latitude and longitde in order to slice it into smaller scenes of cloud fields. At its nadir the data has a nominal resolution of 2 km. As our studied region is located further east between 20°W and 60°W and between 5°S and 30°N, the altitude angles from those locations to the satellite are significantly smaller than 90°. Therefore, the resolution is in the range 2–3 km for most of the domain and is shown by Figure 2.3.
The ABI in its default scanning mode provides a full disk image every ten minutes, which is roughly the time it takes to scan the disk from north to south. As our region of interest is close to the equator we can assume the timestamp of the image to be halfway between the start and end of each scan. This leaves an error below 2 min, which is very accurate considered that we only need the absolute times when comparing with ERA5 parameters that have a temporal resolution of 3 h.

The data can be accessed on AWS via a "json" object containing metadata of the corresponding file. This reduces the required storage capacity from 3.2 GB for a full day netCDF file to 37 MB for a daily json. Specific chunks of the data can then be accessed without downloading the full dataset. However, slicing out by latitude and longitude requires us to compute those coordinates on the full dataset, which renders this method very slow in comparison with the fully downloaded netCDF file. Therefore the files for the studied period of two months were downloaded on a daily basis.
A total of 26 images (0.3 %) is not available on AWS due to transmission failure from STAR[3] or server/network issues at the SSEC[4] with the largest continuous lack of images being 2.5 h on January 6 2020.

2.3. Cloud mask

With the brightness temperature we can identify individual pixels as the temperature of the sea surface (no cloud) or the cloud top temperature. The sea surface temperature can range in our region of interest between 293–302 K. In accordance with other studies (e.g. Bony, Schulz,

---

[3] Center of Satellite Applications and Research, NOAA

[4] Space Science and Engineering Center, University of Wisconsin-Madison

et al., 2020) we define shallow cumulus clouds in the temperature range of 280–290 K leaving a 3 K buffer to the coldest sea surface temperatures, which should avoid misinterpretations on the low cloud end. Everything above 290 K is not considered as shallow cumulus anymore. The binary cloud mask identifies only the shallow cumulus range as cloudy and the rest as non-cloudy. If we ignore higher (cirrus) clouds as we want to study shallow cumuli, we are still left with the ambivalent interpretation of what is beneath a high cloud. In this thesis the region below high clouds is assumed as cloud free, but there are certainly cases where cirrus clouds move above shallow cumulus or clouds that convect deeper than usually can move out of the temperature range. In fact, for two-dimensional brightness temperatures only the top cloud layer can be observed. Our decision to ignore high clouds is discussed in section 4.2.

2.4. Threshold for fraction of high clouds

The decision of the cloud mask for or against low cloudiness under high clouds is ambivalent and introduces errors into the cloud metrics that we want to avoid. If we imagine the extreme case of 100 % high cloud cover, which is seen as a cloudless sky through the cloud mask, it becomes clear that the cloud metrics can be biased depending on the fraction of high clouds. Therefore, images with too many high clouds should be excluded to keep this error small.

We define two kind of thresholds: temperature thresholds and high cloud fraction thresholds. With the temperature threshold we consider everything below that temperature as high clouds. The logical choice is to set the threshold at 280 K as this is the lower temperature bound for the shallow cumuli. Following Bony, Schulz, et al., 2020 a threshold of 285 K can also be used. A third temperature threshold was concluded through analysis of ten days of data (01.02.20 to 10.02.20) on a 10°×10° domain east of Barbados (48°-58°W and 10°-20°N). In the distribution of brightness temperatures of all pixels in all images it shows that the number of pixels decreases with lower temperatures. If we plot the cumulative distribution, i.e. the amount of pixels below a certain temperature, we find a linear trend in the range 283–290 K. By extrapolation we find that around 282 K the amount of pixels below that threshold should drop to zero, although in reality there are still few higher clouds. With this motivation 282 K was used as another temperature threshold.

The second type of threshold defines the minimum fraction of high clouds, as defined by the temperature threshold, where we disregard the image. This threshold should be chosen as low as possible to not distort the cloud metrics. However, a too low threshold will exclude too much of our time series decreasing the statistical relevance of the analysis. The temperature thresholds 282 K and 285 K exclude clouds that are actually considered as shallow cumuli. This can lead to scenes full of shallow cumuli that are excluded from the time series just because the brightness temperatures are rather low in the shallow cumuli range. To avoid this misinterpretation the temperature threshold of 280 K was used in the analyses in this thesis.

Thus, we are left with the choice for a reasonable threshold for the fraction of high clouds. We can see in Figure A.2.2 that cloud fraction and open sky are most affected by high clouds. However, if we acknowledge that more high clouds can often coincide with more low clouds as well, it is not surprising that cloud fraction initially increases with high cloud fraction and the open sky index decreases. From Figure 2.4 we can conclude that indeed the cloud fraction and open sky change drastically for small high cloud fractions. But following the logic of these metrics, we can only say that they are obviously distorted if the mean cloud fraction decreases with increasing high cloud fraction and the mean open sky increases. We see this happening from 25 % high cloud fraction on, which is why we choose this as our threshold value. In scenes of larger high cloud fraction we can expect the high clouds to start dominating the scene. By removing them we still keep 80 % of our data and this threshold is even less restrictive than the one chosen by Bony, Schulz, et al., 2020.

2.5. Cloud metrics computation

Out of the 21 cloud metrics used by Janssens et al., 2021 the mean length scale L_{mean} and cloud fraction cf were chosen for our analysis. To capture as much variance as possible in a

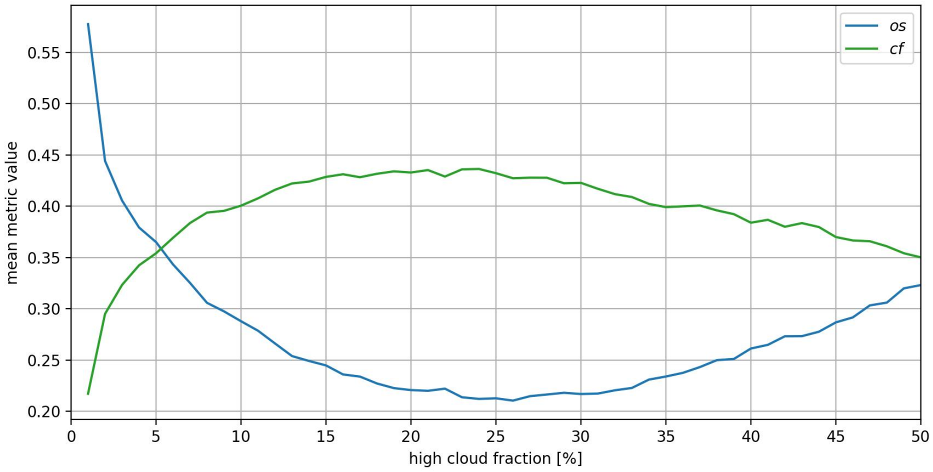

Figure 2.4: Mean values of open sky index and cloud fraction for different high cloud fractions. The mean is calculated in an interval of $\Delta hcf = 1\,\%$ below the given high cloud fraction.

two-dimensional metric space the gradients of the chosen pair of metrics should be orthogonal in metric space. Preferably, a pair of metrics is therefore closely related to the first two principal components (PCs) found by Janssens et al., 2021. The mean object length is a good choice to align well with the first PC, while the open sky parameter is almost parallel to the second PC. However, we chose cloud fraction instead of open sky because it is negatively correlated with open sky and a more robust metric. Further, the two chosen cloud metrics are relevant for the cloud radiative effect, as the mean length scale is correlated with the optical depth of the clouds (Alinaghi et al., 2023; Janssens, 2023).

Other possible pairs of metrics would be L_{mean} and os, N_{objects} and cf or cf and fractal dimension. All the computed metrics are listed in section A.1, but here we focus only on the two used in the further analysis. Cloud fraction is simply the fraction of cloudy pixels from all pixels ignoring undefined ones (NaNs). L_{mean} is the square root of the mean object area in units of pixels of the given satellite image. Thus, we need to scale it with the resolution shown in Figure 2.3 in order to obtain L_{mean} in km-units. For further information on the other cloud metrics it is referred to the supplementary information of Janssens et al., 2021. The code used for computing the above named metrics can be found on GitHub.

For the computation of the metrics we iterated over the satellite images one by one looking for trajectories that are in our region of interest at the time of the image. Then the image is loaded and for each trajectory a 5°× 5° frame is cut out, where the metrics are computed on and attached to the trajectory point. The computation by image was preferred over the computation by trajectory, because loading the image took most of the time in the process. As the images are native on a fixed grid of viewing angles x and y, the lat/lon based frames are slightly distorted in the dataset, while the boundary contains undefined values. For almost all metrics the cloud mask considered these undefined pixels as non-cloudy and only for the open sky index as cloudy. This is no inconsistency because for cloud fraction and open sky the pixels outside the frame are ignored this way.

The frame size was chosen in accordance with Janssens et al., 2021. For a better comparison with the ERA5 parameters, which were averaged on circles of 100 km radius, one could use smaller frame sizes down to 2°×2°. Because of the spatial range in mesoscale patterns between 20–2000 km the smaller frames would only capture the lower part, while very large frames like 10°×10° often contain different types of patterns Stevens, Bony, et al., 2019. The 5°×5° frames are expected to capture patterns related to Sugar, Gravel or Flower. Fish are often too large, but also not useful to capture with a square frame due to their shape.

To get an idea of how the metrics behave on different frame sizes we performed a test with 10 trajectories on 2°×2° and 5°×5° frames. The comparison of the average cloud metric values for both frame sizes reveals that there are roughly 5-6 times as many objects in the bigger frames and the maximum object length scale is larger as well. This is intuitive because the large objects tend to be cut off in smaller frames. Cloud cover and mean object length scale were found to be roughly independent of frame size. Overall, the metrics were less noisy on the larger frames.

2.6. Data postprocessing

The time series of cloud metrics $p(t)$ along the trajectories can be expected to contain signal $s(t)$ and noise $n(t)$:

$$p(t) = s(t) + n(t). \tag{2.5}$$

There are multiple methods to extract a signal from this. To purely reduce the noise in the time series, one can use filter functions like the Gaussian filter or the Savitzky-Golay filter. The former gives a convolution of the time series with Gaussian kernel of width σ, the latter fits a low-degree polynomial to a subset of data points of length Δt and by that estimates the smoothed signal at the central point of the subset. A comparison of both filters showed that a Savitzky-Golay filter has a lower error than a Gaussian filter with $\sigma = \Delta t$. However, a similar smoothing effect is reached with significantly lower σ than Δt, making the Gaussian filter more applicable as it is computationally more efficient.

Another method is to simply take a temporal average over time periods longer than 10 min. The ERA5 parameters have a temporal resolution of 3 h and for comparison the cloud metrics can also be averaged on 3 h intervals. Thereby we neglect possible signals on shorter timescales.

The signal-to-noise ratio can also be improved by averaging over an ensemble of trajectories. Assuming that the cloud metric time series have similar signals $s_1, s_2, \ldots, s_N$ but random noise, taking the mean or the median of that ensemble at every time step increases the signal while the noise cancels out more and more. We expect the signals to be similar for different trajectories, if the trajectories are temporally or spatially aligned or both. This assumes that a possible trend in the ensemble time series is due to the spatial and/or temporal propagation of the cloud fields in the trade winds. While we neglect seasonal differences throughout the two months of trajectories, the local time of the day and the days after the initialization of a trajectory do matter for possible trends and diurnal signals in the time series. Therefore, the temporal alignment chosen in the ERA5 trajectories is already sufficient, as the trajectories were all initiated at the same local time of the day. The spatial alignment is given so far that we only include trajectories that on average move in the south-west direction of the trades. The best spatial alignment is in the region of initialization in the middle of the trajectories. Before and after that region the trajectories converge and diverge, respectively, such that the spatial alignment is a less given there.

2.7. Evolution analysis

We expect the median trajectories to show some kind of trend and eventually oscillations due to diurnality or other reasons. In order to describe the median behavior of cloud metrics and cloud controlling factors over time, we can fit them with analytical functions and compare the fit parameters. To keep it simple, we permit a trend up to second order in time and an oscillation of a given period, delay and amplitude. Although the fit functions are structurally the same, we differentiate between the parameters that describe the cloud controlling factors and the ones that describe the cloud metrics:

$$c_i(t) = a_i \cos\left(2\pi \frac{t - d_i}{T_i}\right) + k_i t^2 + s_i t + r_i \quad \text{for} \quad i = 1, \ldots, n \tag{2.6}$$

$$p_i(t) = \alpha_i \cos\left(2\pi \frac{t - \delta_i}{\tau_i}\right) + \kappa_i t^2 + \sigma_i t + \rho_i \quad \text{for} \quad i = 1, \ldots, m \tag{2.7}$$

Thereby we want to emphasize that the cloud metrics describe the mesoscale and eventually change in a different way than the cloud controlling factors that are large-scale parameters and mainly change because of the Lagrangian perspective.

Especially by comparing oscillation periods and delays of cloud metrics and CCFs we can get insights into what causal relationships are likely and how much the effect in a cloud metric might lag behind the cause in a CCF.

From individual cloud metric time series or their ensemble median we can find general trends that the trajectories moving along the trades have in common. However, while these trends could still be coupled to spatial movement and time, looking at short time tendencies in the space spanned by two (or more) metrics can give us an even more general understanding of how shallow clouds behave in the mesoscale.

In the two-dimensional case we can describe the state of a pattern as a vector $\boldsymbol{p}(t) = [p_1(t), p_2(t)]^T$ with metrics p_1 and p_2. The tendency in between two subsequent time steps at time t with a temporal distance of δt is

$$\delta \boldsymbol{p}(t, \delta t) = \boldsymbol{p}(t + \delta t) - \boldsymbol{p}(t). \tag{2.8}$$

If we couple the tendencies to their origins $\boldsymbol{p}(t)$ in the metric space we can plot a flow field that shows how the patterns evolve with respect to their current state. If this is done for multiple trajectories, we can create bins in the metric space and compute the average of all tendencies that are originated in that bin.

The obtained flow field can then be visually analyzed on its divergence which should have local minima at (meta)stable states.

2.8. Multilinear regression

To investigate the influence of the ERA5 large-scale parameters on the cloud patterns, a multiple linear regression (MLR) of each cloud metric onto the six CCFs was performed. Mathematically this resembles the estimate of the regressors β_j in

$$p_i = \sum_{j=1}^{6} \beta_j c_{ij} + \beta_0 \quad \text{for} \quad i = 1, \dots, n \tag{2.9}$$

with n the total number of data points, p_i the ith metric value and c_{ij} the ith value of the jth CCF. The regressors can vary between the different metrics. The estimate is done on basis of ordinary least squares, thus the sum of the squared residuals

$$S = \sum_{i=0}^{n} \left(p_i - \sum_{j=1}^{6} \beta_j c_{ij} - \beta_0 \right)^2 \tag{2.10}$$

is minimized. Let's denote the regressors that minimize $S(\beta)$ as $\hat{\beta}$ such that

$$\hat{p}_i = \sum \hat{\beta}_j c_{ij} - \hat{\beta}_0 \tag{2.11}$$

with $\hat{p}_i$ the metric values predicted by the regression. To measure the fraction of cloud metric variance explained by the CCFs variance we use the coefficient of determination

$$R^2 = \frac{\sum (\hat{p}_i - \overline{p})^2}{\sum (p_i - \overline{p})^2}. \tag{2.12}$$

Due to possible nonlinear relations between certain CCFs and the cloud metrics we optimized R^2 by replacing the c_{ij} with $\exp(a c_{ij})$ or c_{ij}^a with some constant a. If R^2 increases significantly by this, we can assume that the relation is indeed nonlinear.

We call this regression simultaneous because we assume the values p_i and c_{ij} at the same time and no lags are included. As the metric values are 18 times as frequent as the three-hourly CCFs we can use the instantaneous metric value closest in time to the CCFs or average over the metric values in an interval of up to 3 h centered at the time of the CCFs. Here we chose for the latter option.

Informed by the fit parameters from Equation 2.6 and 2.7 we can also introduce lags if CCFs and cloud metrics with the same oscillation period are shifted against each other. If we then perform the multiple linear regression of the cloud metrics onto the CCFs in question, we can obtain regression coefficients that take the diurnal cycle and how it is transported from the CCFs onto the cloud metrics better into account than the simultaneous regression.

Further, the CCF values were standardized to ensure that the computed regressors give an indication, what CCF the cloud metric is most dependent on. Standardizing means subtracting the mean and dividing by the standard deviation of each individual CCF.

2.9. Removal of large-scale influence

With the results of the MLR we can describe a part of the variance in the cloud metrics by the variance in the CCFs $\boldsymbol{c}(t) = [c_1(t), \dots, c_6(t)]^T$. As long as $R^2 < 100\,\%$ there is a residual term that cannot be explained by the large scale environment of the cloud field. We can assume that there is always a certain portion of noise on the cloud metric time series which is an additive term. The more important assumption however is, if and how the mesoscale self organization attributes to the time series. As a simple guess, which will be discussed in section 4.3, we assume the mesoscale term to be additive as well such that the time series are composed as

$$p(t) = \hat{p}(\boldsymbol{c}(t)) + p_{\text{res}}(t) = \hat{p}(\boldsymbol{c}(t)) + m(t) + r_{\text{noise}} \tag{2.13}$$

with the function

$$\hat{p}(\boldsymbol{c}(t)) = \sum_{j=1}^{6} \hat{\beta}_j c_j(t) + \hat{\beta}_0 \tag{2.14}$$

and its coefficients $\hat{\beta}_j$ as obtained from the MLR. This way, we can simply subtract the CCF-explained part from $p(t)$ to be left with a mixture of mesoscale contribution and noise. The absolute value of this residual does not contain information as the $\hat{\beta}_j$ minimize the sum of squared residuals by definition, but a positive (negative) $p_{\text{res}}(t)$ corresponds to the mesoscale and noise increase (decrease) the value of the cloud metric compared to the case where $p(t)$ would be purely determined by CCFs. In the case where the signal to noise ratio in the residual is good enough we can obtain information on the mesoscales state and its evolution $\partial m(t)/\partial t$. As the function $\hat{p}$ can be obtained with various options from different data averaging intervals to lag regressions, the values of $p_{\text{res}}(t)$ need to be standardized for better comparison.

3

Results

We computed Lagrangian time series of cloud metrics along the ERA5 trajectories. First, we are going to present the ensemble medians of these time series together with a few individual examples. In section 3.2 we show the evolution of the ERA5 parameters, that are often referred to as cloud controlling factors (CCFs). Further, we investigate the memory in the time series by evaluating the decorrelation time scale. The mean tendencies in cloud metrics space are shown in section 3.4 and we discuss the stability of the states in that space. Finally, we perform multilinear regressions on temporally averaged data and on the fitted ensemble averages. We use both to remove the large-scale influence from the time series and study the behavior of the residual signal in section 3.6.

3.1. Ensemble time series of cloud metrics

We begin with presenting the time series we obtained from the cloud metrics computation. We only have cloud metrics computed over the domain shown in Figure 2.1, but most trajectories start and end outside of this domain. Therefore, the number of time steps per trajectory can vary between zero, where the full trajectory is outside the domain or covered by high clouds, up to 931 time steps of 10 min UTC increment (≈ 6.3 d in local time), while the average is 457 time steps (≈ 3 d in local time). Their alignment is shown in Figure A.2.1.

In this thesis both UTC time and local time are used because the trajectories were initially aligned by local hours, which is advantageous for studying diurnal cycles, but the GOES-16 images are available at 10 min UTC time. Local hours obviously change with longitude and in a Lagrangian study of cloud fields the passage of local hours depends on the movement. Here, we assume the average movement of our trajectories of 6.5° westwards per day UTC, which makes 24 local hours equal to 24.5 h UTC. We should mention that the local time obtained from our simple formula by UTC time and longitude is 3–15 min ahead of the true solar time and that the local hours are binned between full hours.

Individually the time series contain a lot of variability on sub-hourly time scales (see colorful lines in Figure 3.1a and 3.1b), that we consider as microscale fluctuations. This is especially true for the mean object length, which can change drastically if a cloud (dis-)appears or cloud objects split/merge and only few cloud objects are present in the frame to equal out the statistics.

In order to get a more general image of the evolution of the time series, we look at the ensemble median at each time step. This median shows a negative trend for the mean object length in the first 72 h of the trajectories from 23 km to 12 km and on top of this a diurnal cycle with a period of 25 local hours (cf. Table 3.1) and an amplitude of 1.2 km. The maxima of this diurnal cycle occur around 05:30 local time in the first half of the trajectories and around 07:30 local time in the second half of the trajectories, while the minima also shift from 20:30 to 21:30 local time (not shown).

In comparison, Vial, Vogel, et al. (2021) found the Flower and Fish patterns peak in their

(a)

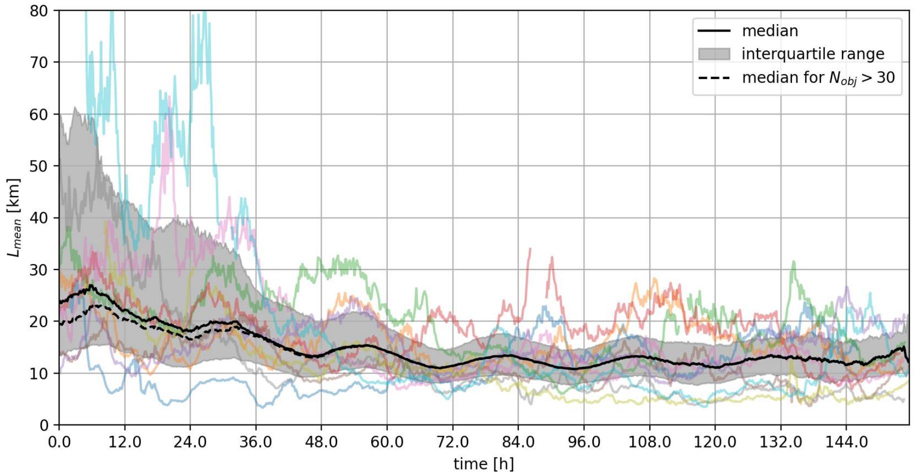

(b)

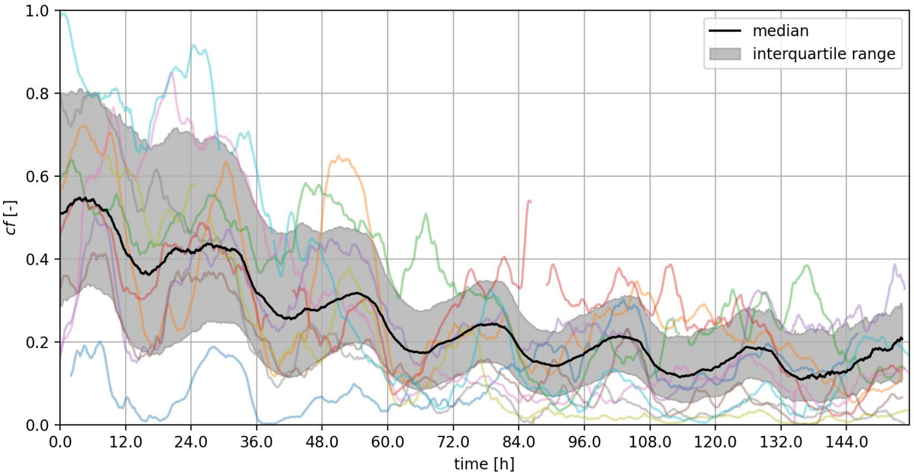

(c)

Figure 3.1: a) Mean cloud object length and b) cloud fraction over time after start of the trajectory. The colorful lines show the evolution along individual trajectories, while the black line is the median of all trajectories at each time step and the interquartile range is shaded. The data points with more than 25 % high clouds (brightness temperature lower than 280 K) were excluded (e.g. the red time series after 84 h). As a statistical variable the mean object length becomes more robust if more objects are considered in the mean. Therefore, the median for scenes with $N_{obj} > 30$ is plotted dashed in comparison.

occurrence at 03:00 and 12:00 local time, while the Sugar and Gravel patterns peak at 14:00 and 00:00, respectively. Thus, our observed maximum in mean object length is between the peak occurrences of the larger object patterns Flower and Fish and the minimum between the peak occurrences of the smaller object patterns Sugar and Gravel.

At the beginning, some of the trajectories have very large mean object length caused by very few objects (not shown). The maximum possible mean object length is related to the number of objects N_{obj} by

$$\max(L_{\text{mean}}) = \sqrt{\frac{A_{\max}}{N_{obj}}} \tag{3.1}$$

with $A_{\max} = 556\,\text{km} \times 556\,\text{km}$ being the largest possible area of a 5°×5° frame. If we make the mean object length more robust by considering only frames with more than 30 cloud objects, the median at the beginning of the trajectories is smaller because frames with a mean object length of more than 100 km are not possible under this condition.

Table 3.1: Fit parameters for trigonometric term of fit function 2.7 on 3 h-averaged cloud metrics. The delay δ and period τ are given in local hours.

p_i	α	δ	τ
L_{mean}	(1.21 ± 0.09) km	(4.3 ± 1.0) h	(25.0 ± 0.3) h
cf	0.042 ± 0.002	(2.6 ± 0.7) h	(24.4 ± 0.2) h

For the cloud fraction we also see a negative trend from 50 % to less than 20 % mainly during the first three days. On top of the trend is a diurnal cycle with a period of 24.4 local hours and an amplitude of 4 p.p. (cf. Table 3.1). The maxima of the diurnal cycle is at 04:30 local time in the first and at 05:30 in the second half of the trajectories while the minima shift from 15:30 to 16:30 local time. This is consistent with Vial, Vogel, et al. (2021), who found that independent of the pattern the peak in cloud cover is during the night time. For LES simulating the trade cumulus regime the results also compare well with the end of our trajectories (cf. Fig. 7.3g in (Janssens, 2023)).

From the time series of mean object length and cloud fraction we learn that some time series start with very large objects and very high cloud fractions, e.g. the light-blue time series in Figure 3.1a and 3.1b. This is mainly the case for trajectories that start at the west coast of the African continent (cf. Figure 2.2b). These can be categorized as transitions from stratocumulus to trade cumulus clouds. They start at cloud fractions of 0.18 to 1 and end between 0.02 and 0.41 (90 % ranges), with a decrease of the median from 0.89 to 0.09 cloud fraction (not shown). Further, the decrease in cloud fraction mainly happens during the first three days of the trajectories. These results are consistent with the observations of Sandu et al. (2010) on the stratocumulus-cumulus transition during the summer months. An example of this transition in one of our trajectories is shown in Figure 3.2.

3.2. Evolution of large-scale parameters

In order to pursue a better understanding of how the cloud patterns are related to the large scale environment, we investigate the evolution of the large-scale parameters. Their ensemble median time series are displayed in Figure 3.3 to 3.5 together with fits of Equation 2.6 onto the medians. We can identify three different types of signals: The ones without a diurnal cycle like the sea surface temperature, the ones with a diurnal cycle (relative humidity, specific humidity, LTS, wind speed) and the semidiurnal subsidence. Whether the specific humidity really has a diurnal cycle or not is open for discussion, but at least the relatively poor R^2 is slightly increased, if the cosine term is considered in the fit.

The ensemble median of SST (Figure 3.3a) has a clear trend to warmer temperatures, which is also visible in the individual time series. The jump at the first time step is because many trajectories do not contribute to the first time step yet, because they are not inside the studied domain, and only trajectories that start already inside the domain (further south-west and therefore over warmer waters) contribute. For the fit we disregard this jump. After roughly 100 h and an increase of 3.5 K the ensemble median reaches a maximum. After that many trajectories move past Barbados and leave our domain and only trajectories that turn to the

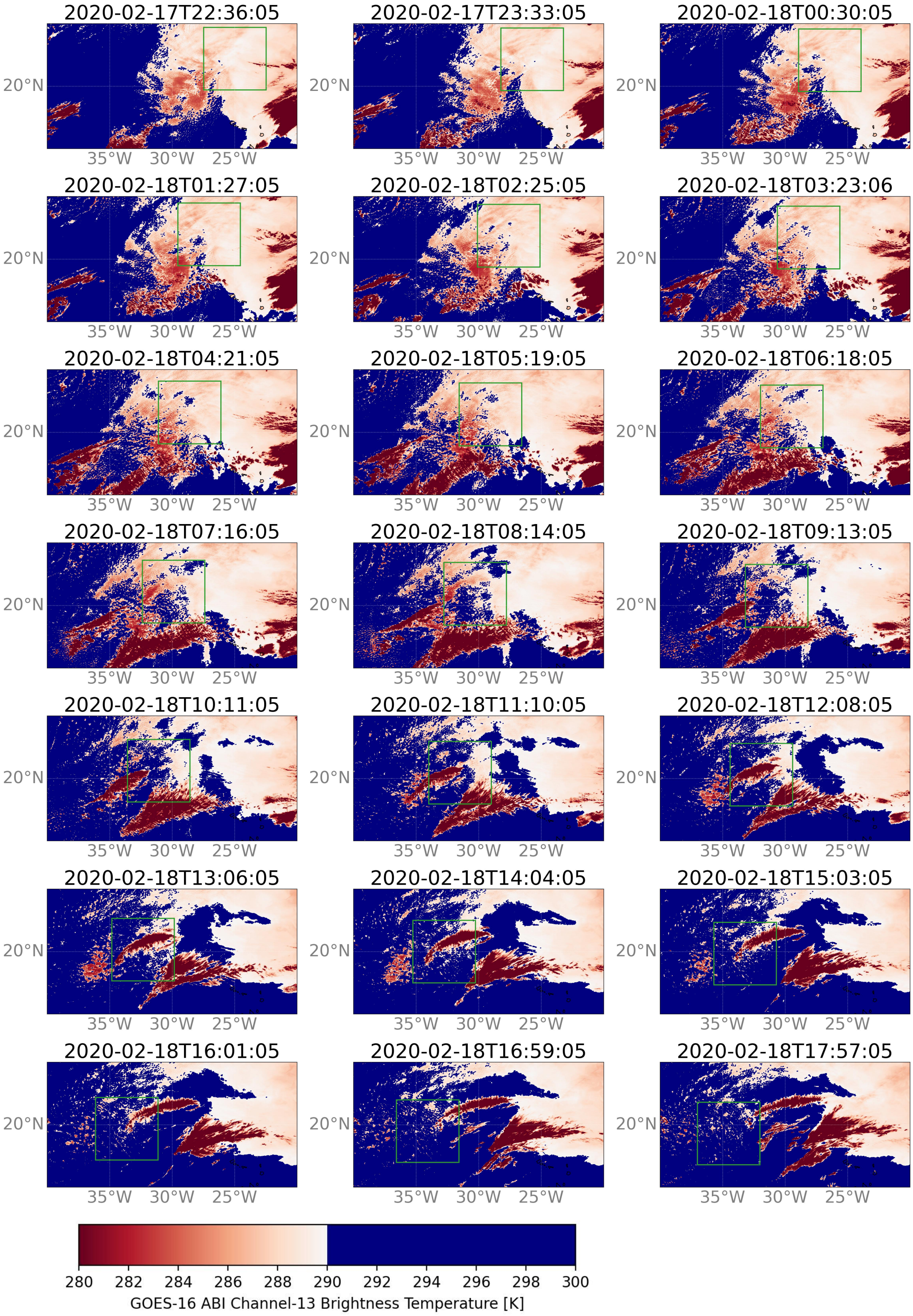
2020-02-17T22:36:05
2020-02-17T23:33:05
2020-02-18T00:30:05
2020-02-18T01:27:05
2020-02-18T02:25:05
2020-02-18T03:23:06
2020-02-18T04:21:05
2020-02-18T05:19:05
2020-02-18T06:18:05
2020-02-18T07:16:05
2020-02-18T08:14:05
2020-02-18T09:13:05
2020-02-18T10:11:05
2020-02-18T11:10:05
2020-02-18T12:08:05
2020-02-18T13:06:05
2020-02-18T14:04:05
2020-02-18T15:03:05
2020-02-18T16:01:05
2020-02-18T16:59:05
2020-02-18T17:57:05

Figure 3.2: Series of snapshots that show the transition of a cloud field (green rectangular frame) from a stratocumulus cloud deck into the trade cumulus regime. The colors show the brightness temperature of clouds at different heights (white is lower, red is higher). Temperatures above 290 K are assumed to be ocean surface (blue).

(a)

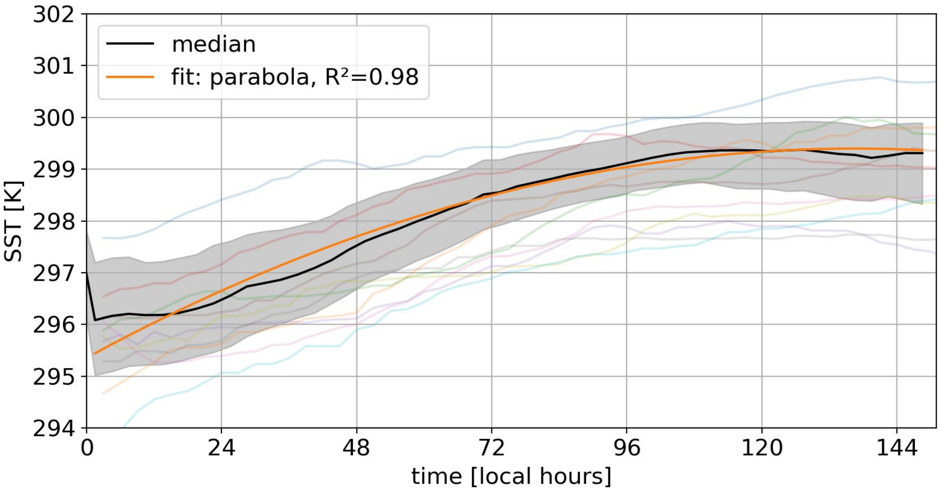

(b)

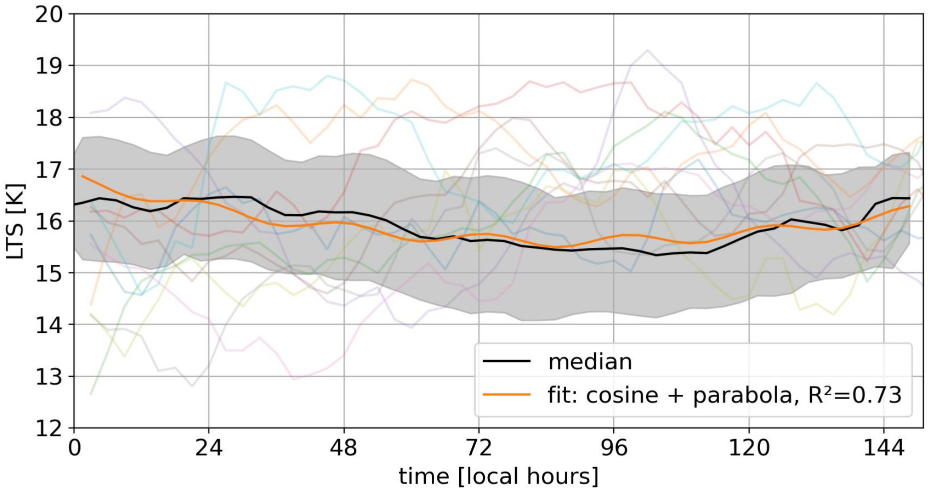

Figure 3.3: a) Sea surface temperature SST and b) lower tropospheric stability LTS over time after start of the trajectory. The colorful lines show the evolution along the same individual trajectories as in Figure 3.1a, while the black line is the median of all trajectories at each time step. The interquartile range is shaded.

north are still taken into account. As the median position does not move far enough north to encounter large changes in SST, the median SST remains at a constant 299.5 K. These values of SST are consistent with Scott et al. (2020), who found the interquartile range of SST in the climatology of the trade cumulus regime to range between 296–300 K, while for stratocumulus it is 290–296 K. Sandu et al. (2010) found a comparable trend in SST, although the sea-surface is roughly 1.5 K warmer during the summer months of their investigation. In Schulz et al. (2021) ten different winter seasons are considered for 72 h back-trajectories and they find a steeper SST trend, increasing from roughly 294 K to 299 K in only three days. Compared to our median trajectory their back-trajectories reach much further north-east, thus covering more of the transition regime between stratocumulus and cumulus.

The LTS (Figure 3.3b) decreases weakly from roughly 16.5 K to 15.5 K after four days and increases back to the initial value in the last two days. We can visually recognize a weak diurnal cycle, also in the interquartile range, but the fit is with a $R^2 = 0.73$ not ideal.
The trend in LTS is much weaker compared to Sandu et al. (2010), where it drops from 18 K below 12 K in six days. If we only consider the trajectories that pass through the stratocumulus regime on the eastern Atlantic (cf. Figure 2.2b) the median LTS drops from 17 K to 15 K before increasing again during the last day, presumably due to the median trajectory moving north. The weaker decrease in stability might also be due to the difference between our observation period in January/February and May until October (period in Sandu et al. (2010)), when the ITCZ is further north.
Schulz et al. (2021) finds that all four classified patterns originate from regions of 15–17 K LTS and after three days Sugar and Gravel patterns decrease to 14 K, while Fish stays rather constant and Flower patterns increase slightly above 17 K. These results are consistent with our interquartile range in the beginning of the trajectories and after 72 local hours.
The relative humidity (Figure 3.4a) below the cloud layer starts to increase after 72 h with a dominant diurnal cycle with a period of 24 local hours and an amplitude of 2 p.p.. Throughout the full time series it is much higher than the lower tropospheric relative humidity that is mostly used in literature (Scott et al., 2020) and therefore hard to compare with. The surface wind speed (Figure 3.4b) increases slightly during the first three days from 7 m/s to 8.5 m/s and then decreases again to 5.5 m/s. The interquartile range of the climatology from Scott et al. (2020) is between 6–7.5 m/s. In our case the upper quartile is at 9 m/s indicating that 2020 was a comparable windy year in the trade region. In contrast, Schulz et al. (2021) finds wind speeds for Sugar and Fish patterns between 7–8 m/s and for Gravel and Flower between 8–9 m/s, which is more in the range of our values.
The subsidence (Figure 3.5a) shows a general negative trend from 50 mPa/s to 35 mPa/s with a diurnal cycle of relatively high amplitude and a period of 12.1 local hours (cf. Table 3.2). This is presumably the second harmonic of a solar atmospheric tide. The variability in individual time series on the timescale of a day is much larger than the variability of the median over the full time series. As for the wind speed, we find higher values for the subsidence than expected from Scott et al. (2020), but roughly in line with the results of Schulz et al. (2021). This, again, might be related to the restriction on the winter season, where the subsidence is expected higher than the yearly average, because the ITCZ is further away.
The free-tropospheric specific humidity is constant at 1 g/kg during the first two days and increases deeper in the trade cumulus regime (day 5) to almost 2 g/kg and then decreases again. A diurnality is almost not visible and the fit parameters for q in Table 3.2 have to be treated with caution. From Sandu et al. (2010) we would expect much values and an increase from 4–7.5 g/kg for the transition into the trade cumulus regime. Our observation is more consistent with the time series of Flower back-trajectories in Schulz et al. (2021).

Most of the fits show a relatively high R^2 while the fits of LTS, subsidence and specific humidity only roughly resemble the actual ensemble medians, which points out that for these parameters more than a simple trend and a diurnal cycle is needed to understand them. However, at least for the LTS we will simplify it with the analytical fit in the following analysis.
The diurnal cycles of LTS and surface wind were also investigated by Vial, Vogel, et al. (2021). They found the climatological mean LTS to peak around 03:00 local time, whereas in our observation the peak shifts from 22:45 in the beginning to 3:15 in the end of the trajectories. This is reasonable because the observed domain in Vial, Vogel, et al. (2021) is reached by most cloud fields in the end of their trajectories. The diurnal cycle of the surface wind speed that peaks at 00:45 in the beginning and around 02:15 in the end of the trajectories is also in agreement with the paper that shows the peak in the climatology around 02:00 local time. The authors further found a diurnal cycle of low amplitude in SST with a peak in the afternoon from ground observations. This is not observed in the reanalysis data along the trajectories.
Now that we obtained parameters on the diurnal oscillations in cloud metrics (Table 3.1) and the large-scale conditions (Table 3.2), we want to compare the two groups. First we want to

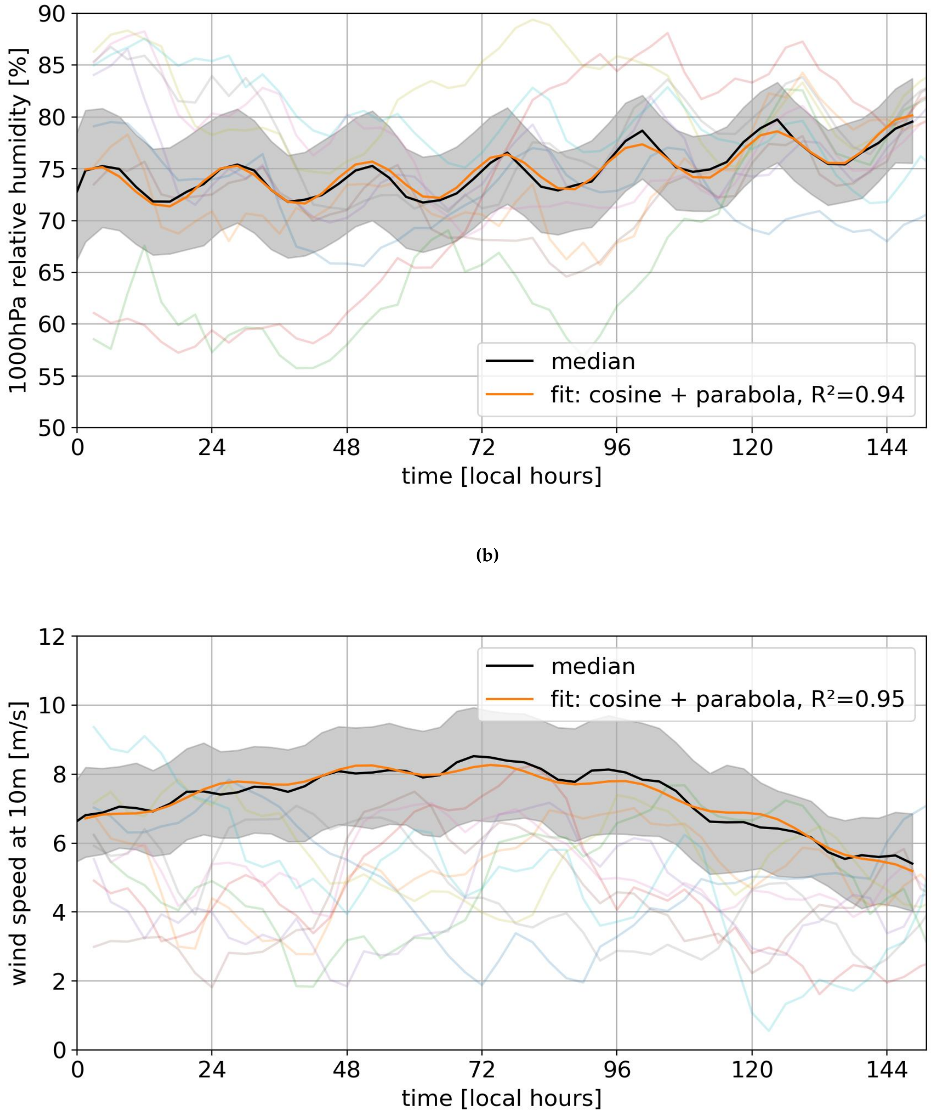

(a)

(b)

Figure 3.4: Same as Figure 3.3 but for a) relative humidity of the sub-cloud layer and b) 10m wind speed. Interestingly all example trajectories show wind speeds lower than the median. This is probably because we picked long time series and the slower the wind speed the longer the trajectories remain in the observation domain.

Table 3.2: Fit parameters for trigonometric term of fit function 2.6 on CCFs. The delay d and period T are given in local hours.

c_i	a	d	T
rel. hum.	(2.0 ± 0.1) p.p.	(3.6 ± 0.6) h	(24.0 ± 0.1) h
LTS	(0.11 ± 0.04) K	(22.7 ± 3.2) h	(24.9 ± 0.9) h
wind speed	(0.18 ± 0.04) m/s	(0.8 ± 1.9) h	(24.3 ± 0.5) h
ω	(-8 ± 1) mPa/s	(2.3 ± 0.4) h	(12.05 ± 0.06) h
q	$(-4 \pm 3) \cdot 10^{-2}$ g/kg	(19.2 ± 4.7) h	(24.8 ± 1.4) h

(a)

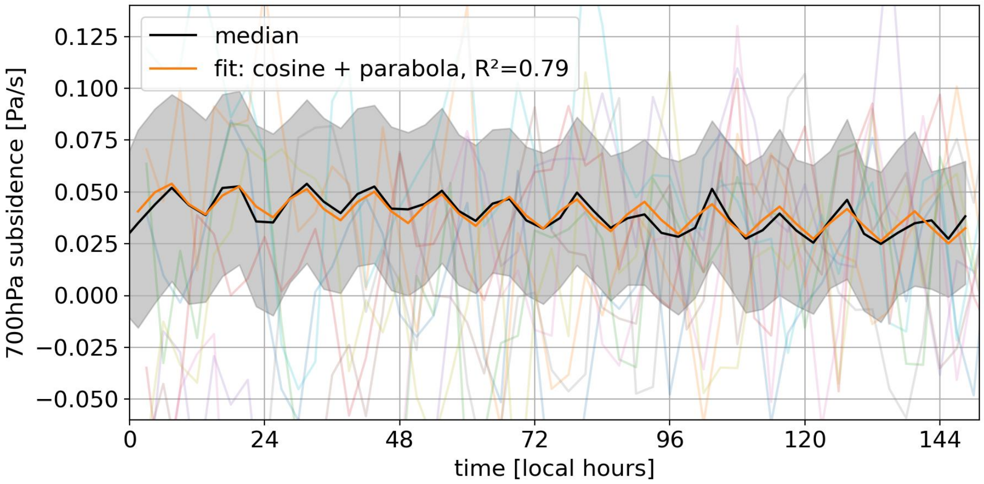

(b)

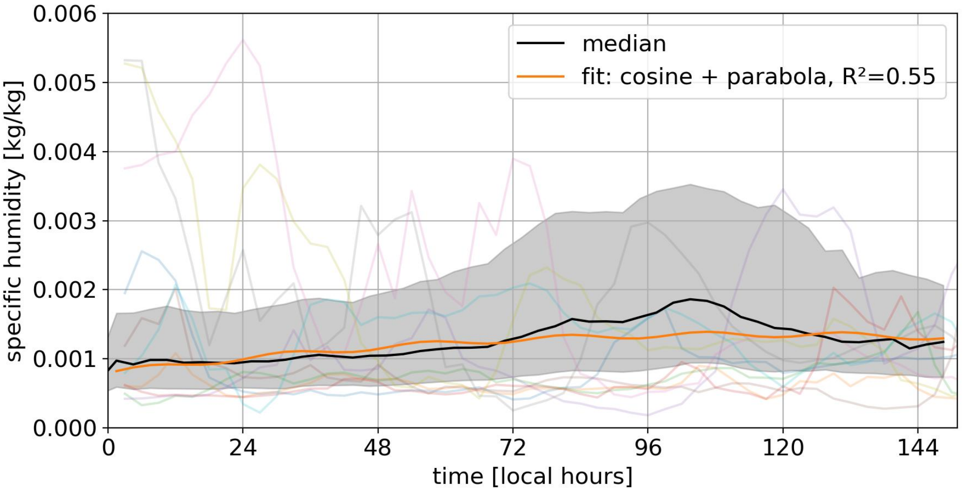

Figure 3.5: Same as Figure 3.3 but for a) Subsidence ω and b) specific humidity.

discuss the observation that the oscillation periods of cloud metrics are above the expected 24 local hours. They might be caused by a shift in the times of solar illumination when moving south during the winter months. If we assume memory or lag in the cloud metrics and CCFs as a reason, the lag would need to increase along the trajectories to actually change the oscillation period. However, if the large scale environment changes between the start and end of the trajectories it is conceivable that the lag increases as well.

If we assume that the diurnal cycle in cloud metrics is caused by CCFs, they should match in their oscillation periods, which are shown with errors in Figure 3.6. For L_{mean}, that has a longer oscillation period of 25 local hours, the LTS is the only parameter that roughly matches the period although it has a very large error and the fit is not very accurate. The oscillation of cloud fraction is matched best by the period of wind speed. The relative humidity is the only one with the expected oscillation period of 24 local hours, which is slightly too short to match with

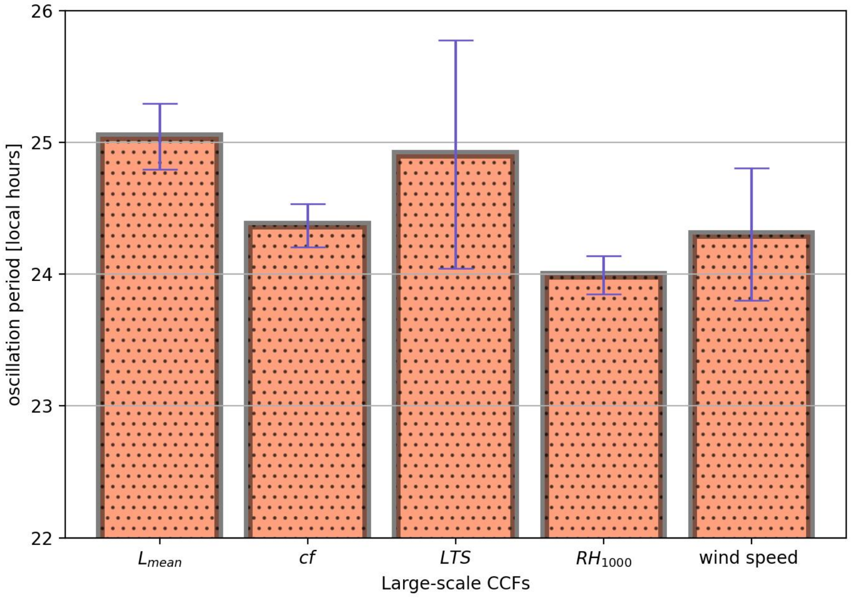

Figure 3.6: Oscillation periods of diurnal cloud metrics and CCFs obtained with errors from fits using non-linear least squares.

the cloud fraction.

Oscillation periods above 24 h Next to the oscillation period the phase in the diurnal signal should also match. If we assume that LTS causes the diurnal cycle in L_{mean}, the difference between the two phases can be seen as a delay between the cause in LTS and the effect in L_{mean}. The median of mean cloud object length is 5.6 ± 4.2 local hours delayed against the LTS (cf. Table 3.1 and 3.2). The delay between cloud fraction cf and wind speed is not significant (1.8 ± 2.6 local hours). We do not expect cloud controlling factors to lack behind the cloud metrics, but compared to the three-hourly average the delay is short enough to not be used as proof against a causality between relative humidity and cloud fraction. However, the lag and the different oscillation periods together place a question mark behind a causal effect that might just be a correlation.

3.3. Memory in time series

In any time series analysis looking at the autocorrelation in the time series is an important component to see how a time series is correlated with its own lagged version, i.e. how much memory it has of its previous values. The mean autocorrelation functions of the two cloud metrics and our six large-scale parameters is shown in Figure 3.7.

From Figure 3.7 we can conclude that the memory in sea surface temperature is the longest while the memory of the cloud metrics is significantly shorter. The other CCFs have a memory equal or slightly longer than the memory of cloud fraction, except for the semidiurnal subsidence. The errorbars in 3.7b show that the central 50 % of decorrelation times of the time series already have a wide spread such that almost all of them overlap partially except L_{mean} and SST. Our three-hourly averaged time series are still correlated slightly as the decorrelation times are all longer than 3 h. Daily data would be uncorrelated, but it would not capture the change in cloud metrics appropriately anymore, which happens on timescales of 4–9 h. Because LTS, relative humidity and wind speed change almost as fast, timescale separation between these large-scale parameters and the cloud patterns becomes unfeasible. We should note, that the displayed decorrelation times might differ from the Eulerian decorrelation. They also contain information of the spatial decorrelation length because of the movement of the cloud fields of 32 km/h on average. Therefore, the short decorrelation time of the large-scale parameters might just be a

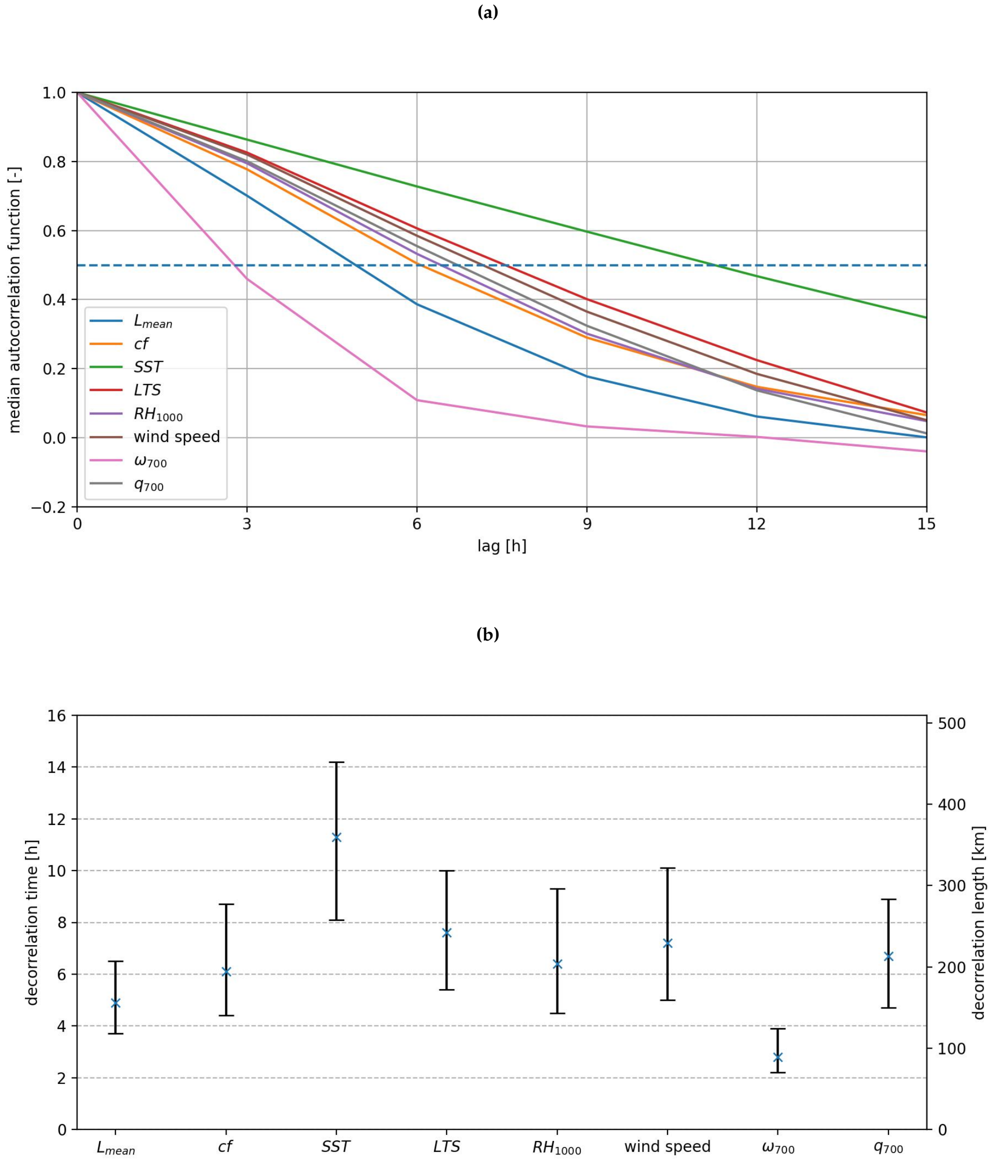

Figure 3.7: a) Median of autocorrelation functions of cloud metrics and cloud controlling factors for lags from 0–15 h in steps of 3 h as the three-hourly averaged time series were used to make the autocorrelations of cloud metrics and CCFs comparable. The decorrelation time is reached when the autocorrelation falls below 0.5 (dashed line). b) Median decorrelation time with the decorrelation times of the first and third quartile as errorbars.

short decorrelation length that shows as a time scale in the Lagrangian framework. On top of that comes the diurnal solar forcing that keeps changing these parameters. Independent of the reasons, the cloud metrics follow the change in their environment almost immediately.

3.4. Diurnal cycle in cloud metrics space

Mesoscale patterns exhibit far greater variance than any single cloud metric can capture. In fact, Janssens et al. (2021) has shown that 82 % of their variance is explained by four principle components, making the state space of a mesoscale patterns four dimensional. In our analysis with two cloud metrics we therefore study the projection of this four dimensional space onto

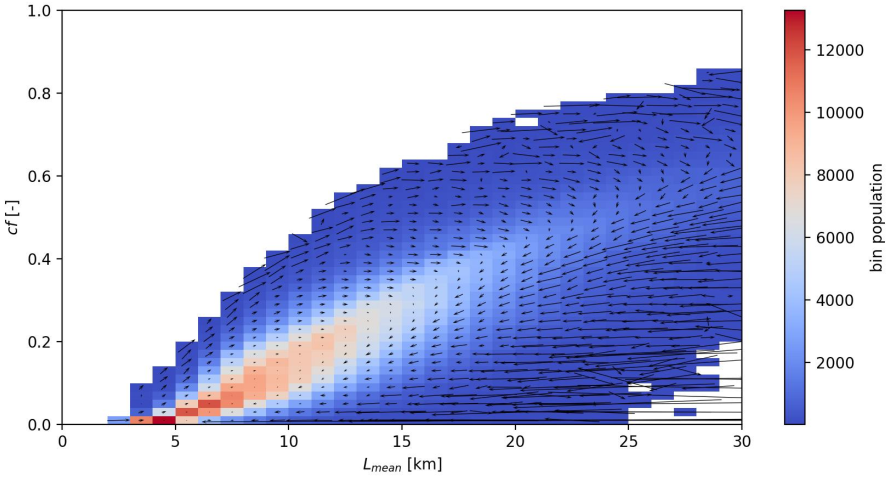

Figure 3.8: Mean tendencies in cloud metric space of mean object length and cloud fraction. The arrows show the mean change per hour of cloud patterns that are located within the corresponding bin. The individual tendencies were obtained for every 10 min increment along all trajectories. The background color displays the number of data points per bin.

the plane spanned by mean object length and cloud fraction. According to Janssens et al. (2021) the plane spanned by the mean object length scale and the void size (open sky) has a cumulative explained variance of 31 %. As explained in section 2.5, we found cloud fraction to be more robust than open sky and due to their negative correlation we assume that our two cloud metrics capture a similar amount of variance.

We can show the mean short-timescale tendencies in a flow field, following the method described in section 2.7. Looking at the mean flow field of cloud patterns in Figure 3.8, a large cycle can be recognized. The cloud fields initially develop from small object sizes and low cloud fractions to higher cloud fractions, whereby the object size also increases. After reaching a maximum cloud fraction, the existing clouds merge to form even larger objects, while the cloud fraction remains constant. Subsequently, both the object length and cloud fraction decrease, with the cloud fraction reaching its minimum prior to the mean object length. If we compare this cycle with the diurnal cycle seen in the ensemble medians, we can identify the upper right corner as the morning hours the descend in both metrics as the hours around noon, the lower left corner as the evening and the increase in both metrics as the night. However, the cycle in the flow field has a larger amplitude than the actual diurnal cycle of most of the time series and can be seen as a composite out of all diurnal cycles. From the upper right corner, cloud fields with larger objects and higher cloud cover transition into the cycle. This transition extends in a much longer tail than shown here. Once a cloud field reaches the large cycle it becomes very unlikely to reach large mean object lengths again. Thus, this transition appears irreversible in the time series along the trades and can be interpreted as the transition from Stratocumulus to Cumulus again.

Cloud fields occur most frequent at the lower end of the cycle (small L_{mean} and cf) and in the center of the cycle, where the mean tendencies almost vanish. The bin population can be disassembled into two factors: the amount of trajectories that pass through the bin and the average time the trajectories spend inside the bin (cf. Figure A.2.4). Most trajectories pass through the bins at roughly 12 km and 20 %, which is consistent with the ensemble medians, and they stay in those bins on average 1 h. Below 6 km less trajectories pass through the bins (by at least a factor of two), but the trajectories spend a significantly longer time inside the bins up to 5 h.

The vanishing mean tendencies can have multiple reasons. One possibility is that all tendencies are almost zero, the state is rather stable and cloud fields develop only slowly. On the other hand, they could cancel each other out on average, which would make the state (symmetrically) unstable. If both are true, we could describe it as a (meta-)stable state. The bins with small absolute tendencies start below 12 km mean object length, with the smallest absolute tendencies around 5 km and below. At larger L_{mean} the mean tendencies are small due to mutual cancellation. Different trajectories pass here at different phases of their diurnal cycle. The most stable bin is indeed the one with the highest bin population. This almost cloud-free state is reached by 471 trajectories, presumably most of them during the evening of their diurnal cycle. The same figure with mean tendencies after Gauss-filtering the sub-hour variabiliy[1] is shown in Figure A.2.3. The main difference is that the tendencies in L_{mean} are significantly weakened at some places in pattern space. Thus, the mean tendencies in those bins were dominated by fast changes in L_{mean}, which are averaged out by the filter, leaving a symmetric distribution of tendencies that cancel each other.

3.5. Dependency on large scale environment

After analyzing the flow field of the evolution of mesoscale cloud fields in the trades, we want to investigate what causes the patterns. The assumption in Equation 2.13 is that the three scales of cloudiness are additive to each other. The large-scale conditions lay the foundation, the mesoscale self-organization can add variance of higher frequencies and the microscale adds variance on even shorter time scales, for our satellite mainly perceived as noise. We are going to test this assumption as well. In this section, we analyze what part of the mesoscale variance is imposed by the macroscale. Therefore, we perform multilinear regressions (MLR) from CCFs onto the cloud metrics. In order to do that, we first average the cloud metrics over intervals of three hours onto the UTC times of the three-hourly CCFs and perform the MLR on the resulting dataset (subsection 3.5.1). In subsection 3.5.2 we then perform the MLR on the analytical fits found in section 3.1 and 3.2.

3.5.1. Multilinear regression onto time series of cloud metrics

Multilinear regression as explained in section 2.8 can predict the coefficients $\{\beta_0, \beta_1, \ldots, \beta_6\}$ of our CCFs (plus a constant β_0) in a linear equation like 2.9. Because we can not assume all CCFs have a linear relation with the cloud metrics we also investigated power laws and exponentials. A significant increase in explained variance was found, if the contribution of SST is considered to be exponential. Thus, in the following we try to find the coefficients in:

$$p_i = \beta_1 \exp\left(a \cdot SST\right) + \beta_2 LTS + \beta_3 RH + \beta_4 v_{\text{wind}} + \beta_5 \omega + \beta_6 q + \beta_0 \tag{3.2}$$

with factor a being optimized (maximize the R^2 of the MLR) to −1 for L_{mean} and to −0.4 for cf. This exponential relation reminds of Clausius-Clapeyron which tells us that the saturation pressure of water vapor exponentially increases with temperature. As a consequence, warmer air can contain more water vapor before condensation sets in and the probability of cloud formation reduces exponentially with increasing temperature. To put it differently, although, the latent heat flux (evaporation) increases with SST, the heat that is set free at cloud height due to condensation drives the entrainment of drier air from above, such that the clouds become thinner.

In Figure 3.9 it becomes clear that the sea surface temperature plays a dominant role when it comes to the instantaneous prediction of cloud metrics from CCFs. The explained variance is 57 %, if we use all six regressors, but remains the same if we reduce it to just SST and LTS, the second most influential one. For a linear SST the explained variance ist only 23 %. The exponential SST is positively correlated with L_{mean} while the stability is slightly negatively correlated.

In contrast, in LESs of the idealized Botany cases (Jansson et al., 2023) subsidence and surface

---

[1] The bandwidth of the Gaussian filter is 30 min

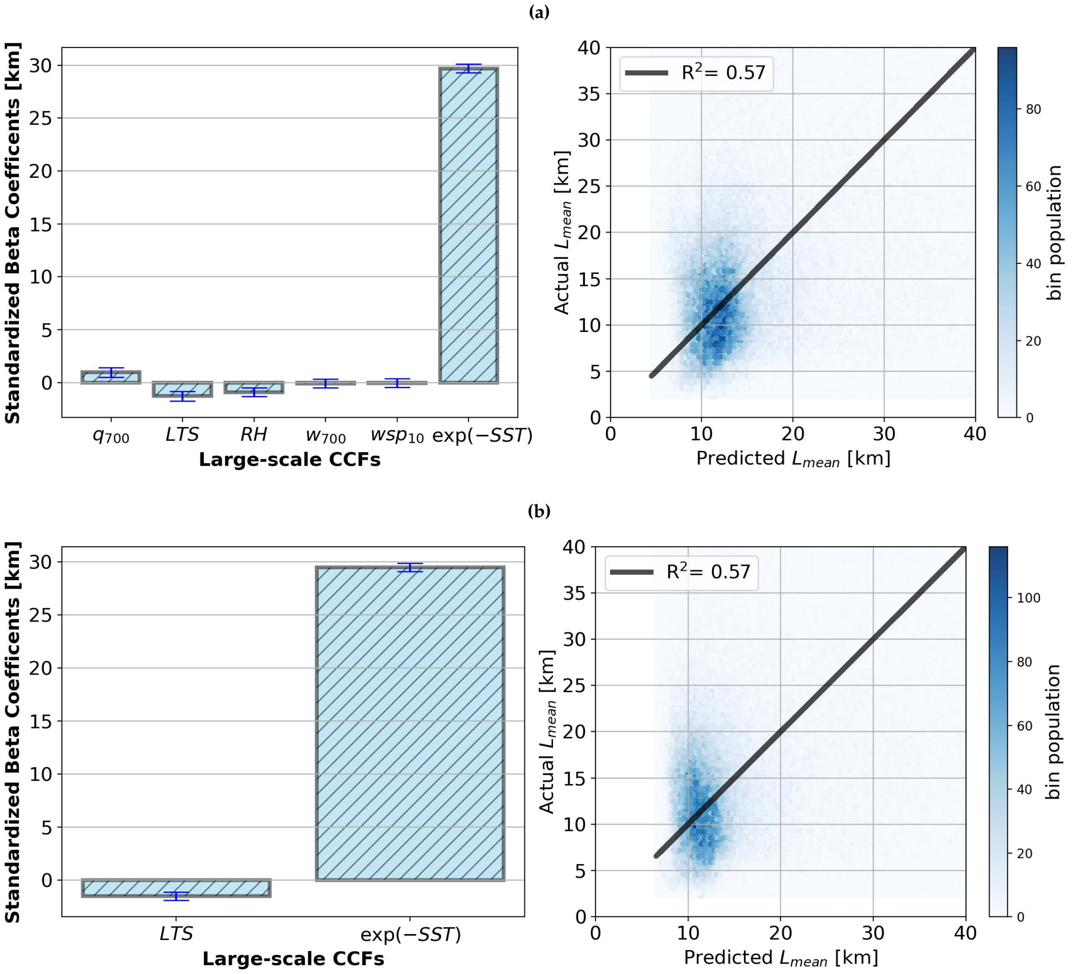

Figure 3.9: Results of multilinear regression of L_{mean} onto a) all large-scale parameters and b) the two most important ones. The contribution of SST is considered exponential with $\exp(-SST)$. On the left panel the standardized regression coefficients are shown per CCF and on the right a density plot shows the distribution of data points around the ideal line where the predicted metric is equal to the actual metric.

wind are found to be most influential for the cloud size of shallow cumuli, while temperature and stability do not play a role[2]. The difference between our observations and the simulations is, that we cannot fix the macroscale and let the system equilibrate, but our cloud fields see a ongoing change in the macroscale. Further, the importance of SST might be reduced if we reduce our domain to the trade cumulus regime, where the large cloud decks from the stratocumulus to cumulus transition and the gradient in SST would disappear.

For the cloud fraction the SST is also dominant although less than for L_{mean} (Figure 3.10). The explained variance of 55 % is also reached after we reduce the regressors to the three most important ones: relative humidity, wind speed and SST. The exponential SST and the wind speed are positively correlated with cf while the relative humidity is negatively correlated. If the SST contribution is assumed linear, 48 % of the variance is explained. Interestingly the increase in R^2 from linear to exponential regression in SST is much more significant in L_{mean}. It remains as a question for future analyses, if this has a physical reason.

In Botany, cloud fraction is positively correlated to wind speed, free-tropospheric humidity and to second order larger stability. It is also negatively correlated with subsidence. However, the

---

[2] These results come from personal communication with P. Alinaghi and are not published by the end date of this thesis.

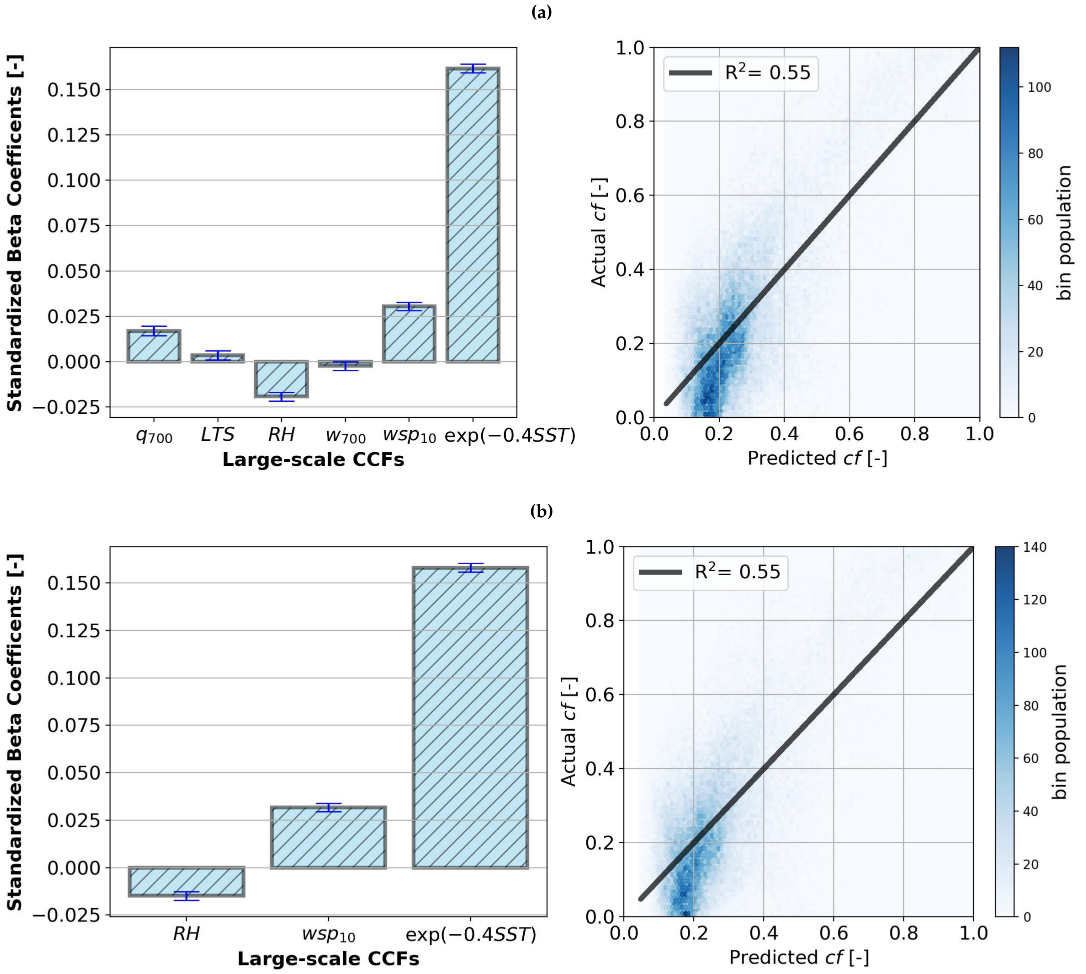

Figure 3.10: Results of multilinear regression of cloud fraction onto a) all large-scale parameters and b) the three most important ones. The contribution of SST is considered exponential with $\exp(-0.4 \cdot SST)$. On the left panel the standardized regression coefficients are shown per CCF and on the right a density plot shows the distribution of data points around the ideal line where the predicted metric is equal to the actual metric.

subsidence in Botany is defined in the cloud layer and not in the free-troposphere as in our data. Note that at larger wind speeds the cloud fraction increases. This is consistent with the results of Bony, Schulz, et al. (2020), who showed that under conditions with stronger winds Flower and Gravel occur and Fish and Sugar, if the winds are less strong. Flower and Fish have comparable cloud fraction and mean object length, but Gravel patterns have larger cloud fractions than Sugar patterns. If L_{mean}, in contrast, is uncorrelated with wind speed we would expect Sugar and Gravel to be equal in mean object length, which is the case if we follow Bony, Schulz, et al. (2020).

In our further regressions we will neglect the specific humidity q and subsidence ω as they don't explain much additional variance in the cloud metrics.

If we use the obtained β-coefficients to predict the time series of cloud metrics from the time series of CCFs, we can compare the ensemble medians of the original time series and the ones that were regressed. This is shown in Figure 3.11. For both cloud metrics the median of the regressed time series stays inside the interquartile range, but it does not capture the diurnal cycle of the metrics. This would not be surprising if some CCFs would not follow a diurnal cycle themselves, as we demonstrate in section 3.2. The influence of CCFs with a diurnal cycle is obviously underestimated in the regression over all temporally averaged time series.

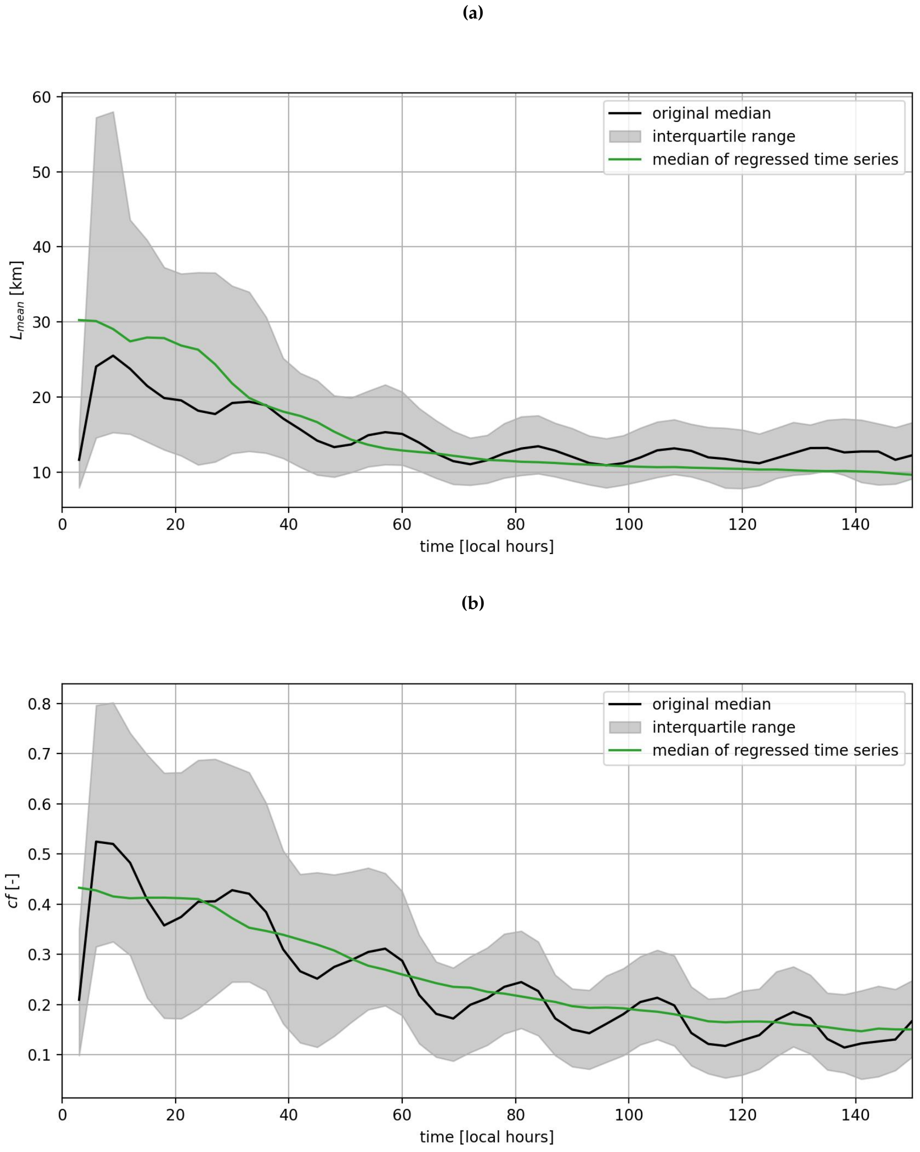

Figure 3.11: Comparison of the median of the original time series and the ones regressed from MLR on the 3-hourly averaged data for a) mean object length and b) cloud fraction.

The same regression as above, with all CCFs, was performed onto datasets, where CCFs and cloud metrics were averaged over intervals longer than 3 h, ranging up to averages over the full time series (144 h) and thereby average out diurnal cycles in cloud metrics and large-scale parameters. The change in R^2 for these regressions is shown in Figure 3.12. The variance of mean object length is best explained if we look at 24 h-averages. The value of R^2 can increase, if the variance in cloud metrics becomes smaller while the variance in the CCFs is constant or decreases less than in the cloud metrics. Thus, at the timescale of a day we reduce the variance in L_{mean} more than the variance in CCFs. Because SST is the most important CCF, we can explain this result by the absence of a diurnal cycle in SST. For longer averaging intervals, the explained variance decreases except at 96 h-averages. As we require longer averages, more and more trajectories are not long enough anymore and are neglected in the regression. This can reduce the variance in the cloud metrics as well, leading to a higher R^2, if the variance in CCFs is not reduced by the same amount.

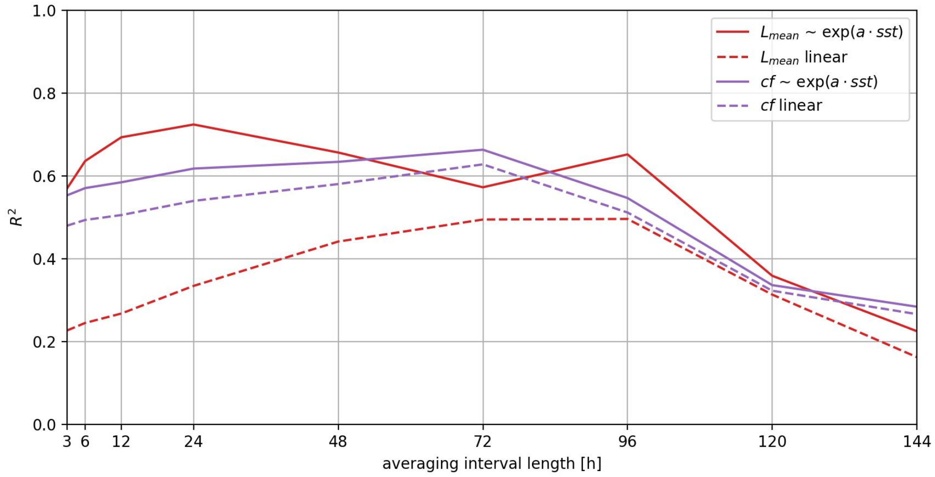

Figure 3.12: Explained variance of MLR on temporally averaged time series data. Averages are computed over temporal intervals of different lengths ranging from 3 h to the full trajectory length of almost a week in some cases. Dashed are values for MLR with linear contribution of SST in comparison to the exponential ones.

For the cloud fraction as well as for the regressions linear in SST we see a maximum in R^2 at three- to four-day-averages. This indicates multi-day-variability that needs to be averaged out to increase the R^2, but the reason for this is unknown.

3.5.2. Multilinear regression onto fitted ensemble medians

Now we will perform the regression onto the fits on the ensemble medians discussed in section 3.2. The fits are reduced in complexity compared to the temporal averages of all time series. First, taking the median removes noise and reduces the variance of the data significantly. Second, by fitting a rather simple analytical function we reduce all the variables of the regression to five independent fit parameters. Therefore, we expect a higher explained variability for this regression, because we basically regress a climatology instead of the variability of individual time series. On the other hand, three of the five fit parameters for each regressor and the cloud metrics describe the diurnal cycle. This way the diurnal cycle plays a more important role in finding a good regression here, which the previous regression still lacked (cf. Figure 3.11).

In Figure 3.13a the 6 hour delayed LTS was used as a regression coefficient as the phase difference between LTS abd L_{mean} is (5.6 ± 4.2) h (cf. Table 3.1 and 3.2), but CCFs are available in steps of 3 h. Without the delay in LTS the regression reaches an explained variability of 87 % instead of 98 % (not shown), with a larger influence of SST, comparable to Figure 3.9. This is because of the phase shift of roughly $\pi/2$ between the diurnal cycles of the immediate LTS and L_{mean} that makes both seem rather uncorrelated (or even negatively correlated). The delayed LTS has about equal influence with the exponential SST. From the evolution of the two CCFs we can conclude that LTS causes the diurnality while the SST controls the trend.
The effect of LTS on L_{mean} is consistent with Bony, Schulz, et al. (2020). There, they found Flower and Fish patterns prevail for a stronger inversion (thus higher LTS), which have larger mean object lengths than Sugar and Gravel. Nevertheless, we need to mention that the uncertainty in the phase shift between LTS and L_{mean} is very large, which is due to the relative poor fit of LTS.
For cloud fraction in Figure 3.13b we recognize that the exponential SST still has the largest regression coefficient. The variance of the diurnal cycle is split up between wind speed and relative humidity. One of them alone cannot fit the diurnal cycle of cloud fraction very well, as the oscillations in wind speed are too small in amplitude and the relative humidity is slightly delayed to cloud fraction and has a small frequency mismatch. However, taken together

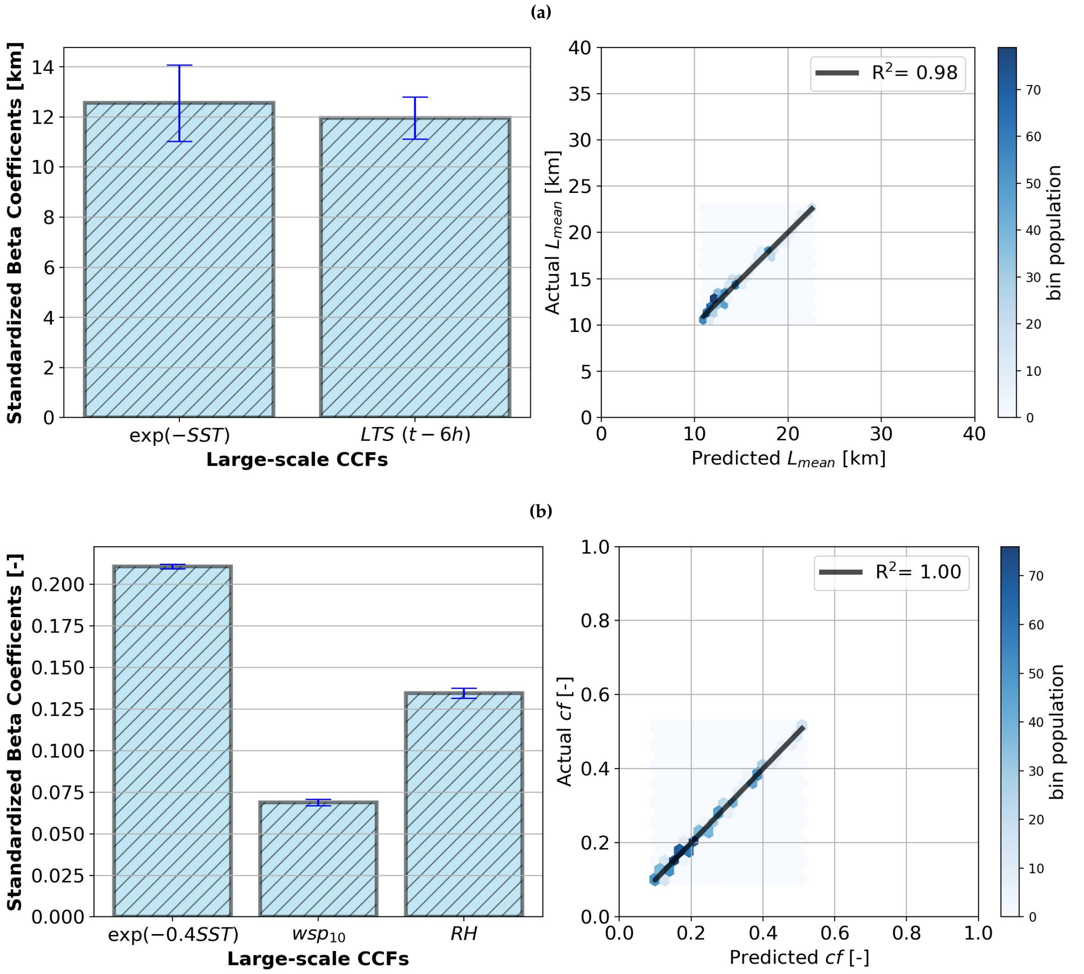

Figure 3.13: Result of MLR on fitted ensemble medians for a) mean object length and b) cloud fraction. On the left panel the standardized regression coefficients are shown per CCF and on the right a density plot shows the distribution of data points around the ideal line where the predicted metric is equal to the actual metric.

they give an almost perfect regression on the fitted functions. Let us now use the regression coefficients of this regression, where diurnality is more pronounced and the resulting signs of the correlations are consistent with other studies, and try to predict the three-hourly averaged cloud metrics from the corresponding CCFs. In Figure 3.14 the medians of the temporally averaged metrics are shown together with their fits and compared to the ensemble medians of the time series that we predicted from the regression coefficients found in Figure 3.13. For the mean length scale the regression with the delayed LTS and SST follows the trend rather well and also captures some features of the diurnal cycle, due to the larger regression coefficient of the delayed LTS that matches the frequency of diurnal oscillation with the mean object length. It only starts at later times, because before we have no information on the six-hourly lagged LTS before. The trend in LTS, however, causes a positive bias for the second and third day of the time series. This might be because of using the same regression on the stratocumulus and the cumulus regime. This would only be valid, if the processes that control the clouds are the same in both regimes. Here we find another indication that this is not the case.

The median cloud fraction is followed very well by the median of regressed time series, especially in the center of the time series, where noise is the lowest as the most trajectories are considered in the medians. We recognize only a small phase difference between the two medians at the end of the time series, that is caused by the slight frequency mismatch of

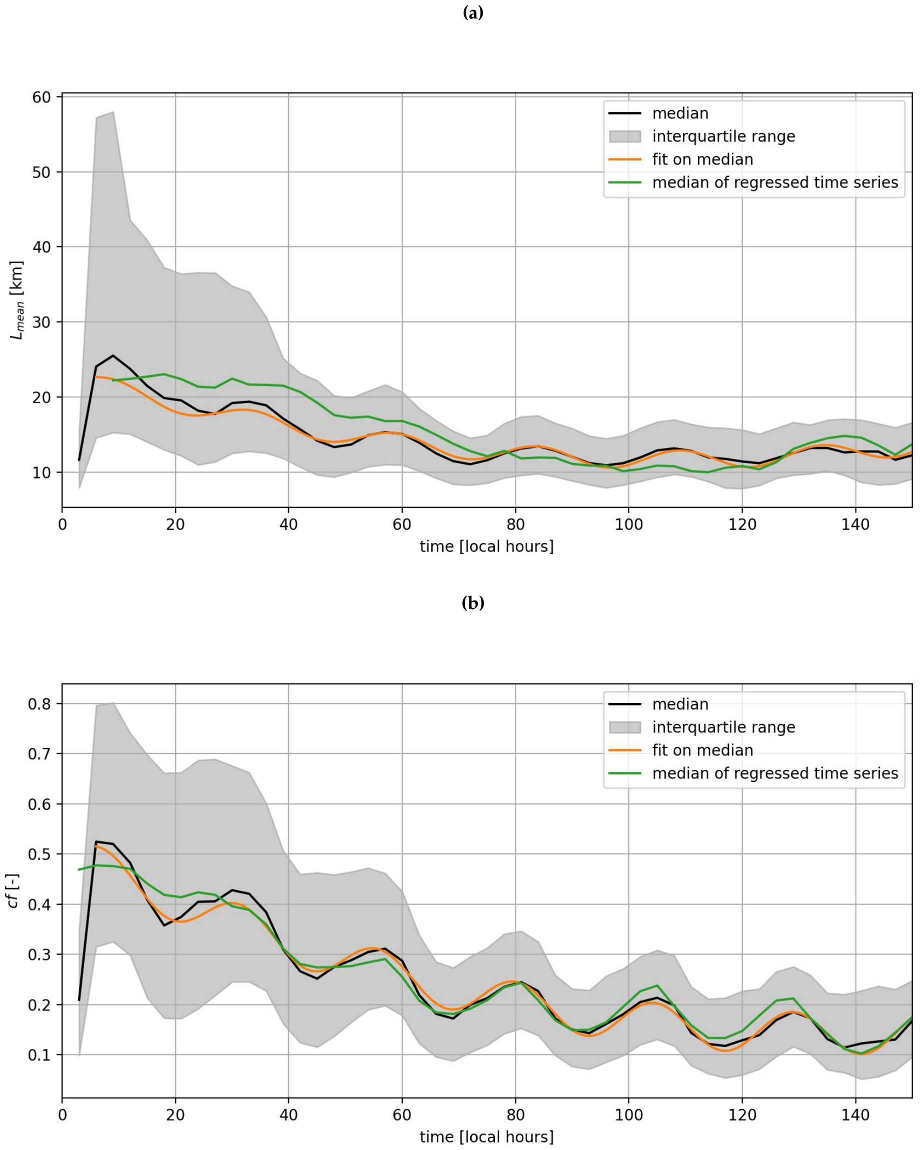

Figure 3.14: Comparison of the median of the original time series (black) with its fit (orange) and the median of the ensemble of regressed time series using the same regression coefficients (green). For both cloud metrics the fit ignored the first data point, as the jump in the metric value is due to a sudden increase in the number of trajectories considered in the ensemble median (for most trajectories the first few hours are cut off). The fit parameters are shown in Table 3.1.

the relative humidity. From these results we can conclude that we are able to explain the trend mainly by a change in sea surface temperature and the diurnal oscillations of the mean object size by the lower tropospheric stability and of the cloud fraction by wind speed with an uncertain contribution of relative humidity. With this knowledge we can look at the residual variance in the mesoscale patterns.

3.6. Residual evolution in cloud metrics

We performed two regressions, one on temporally averaged time series data and one on the fitted ensemble median of these time series with reduced noise and increased importance of diurnality as explained in the previous section. For both we want to see how the residual signal

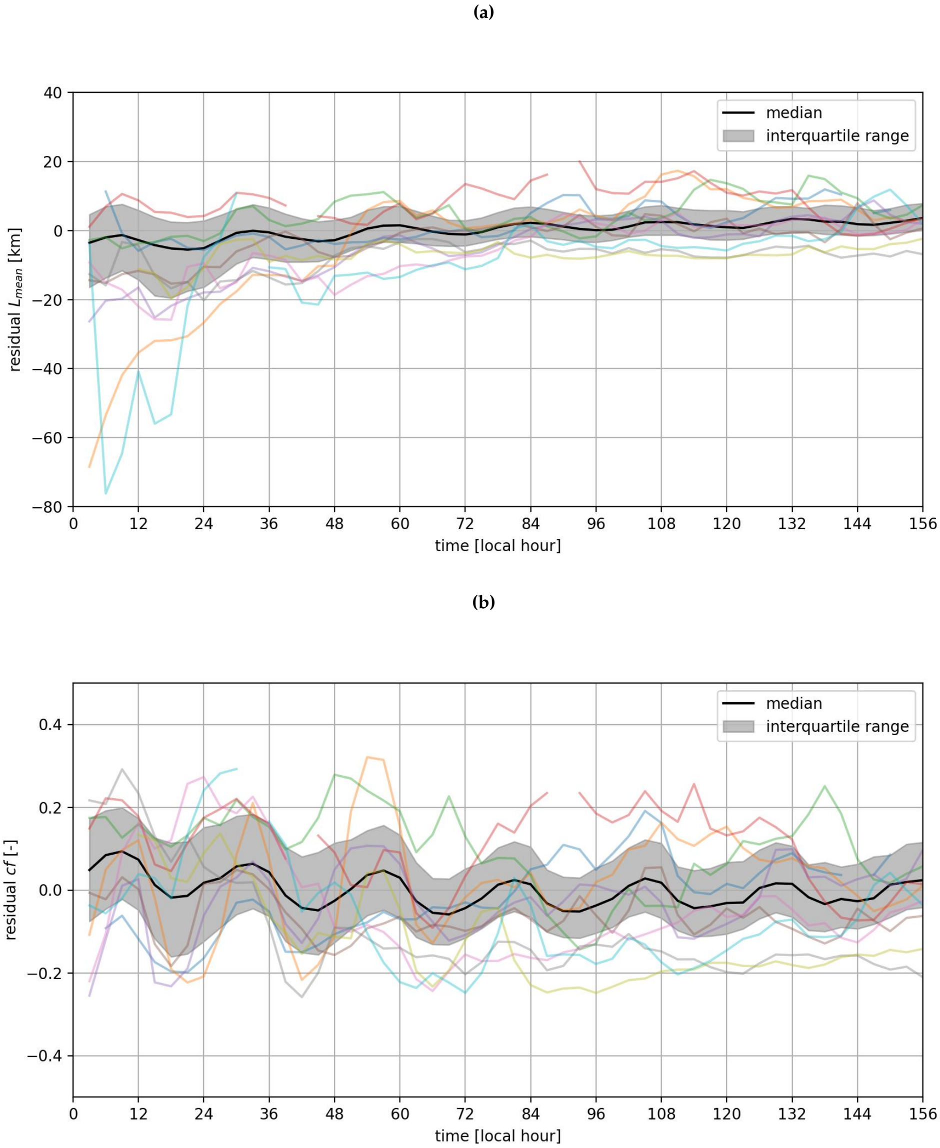

Figure 3.15: Residual cloud metrics a) mean object length and b) cloud fraction over time after the start of the trajectory, where the metrics predicted from the full data regression are subtracted from each time series. The colorful lines show the evolution along individual trajectories, while the black line is the median of all trajectories at each time step and the interquartile range is shaded.

in cloud metrics space looks like and what we can conclude from that for a possible mesoscale self organization.

First, we look at the residual of the full data regression. In Figure 3.15 we see again that the full data regression does not capture the diurnal cycle of the cloud metrics that still occurs strongly in the residual signals. The trend is removed very well, such that the oscillations are now around zero with a very slight increase in residual L_{mean} and decrease in residual cf over the full length of the time series. From the individual time series we can see that the very large objects are overestimated in size by the regression as well as smaller mean object sizes that happened to be above colder SST. This hints, that although the trend of SST is removed rather well, the exponential might be too steep for L_{mean}. On the other hand, large objects tend to be cut off by the boundary of the frame and thereby be negatively biased in the metrics.

If we compare the residual signals after removing the regression on the fitted medians, displayed

(a)

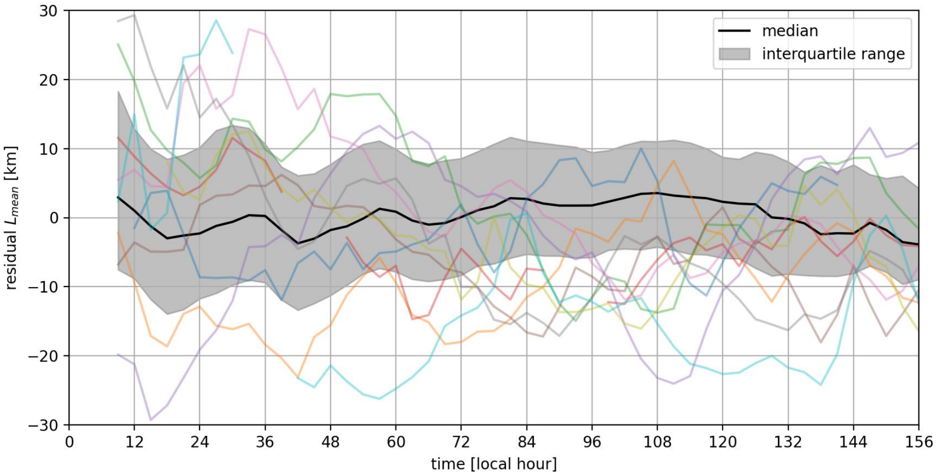

(b)

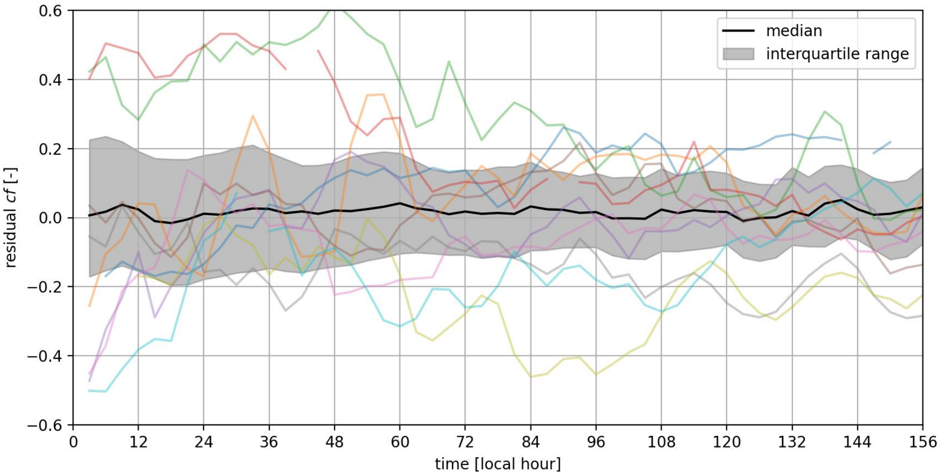

Figure 3.16: Residual cloud metrics a) mean object length and b) cloud fraction over time after the start of the trajectory, where the metrics predicted from the regression on fitted ensemble medians are subtracted from each time series. The colorful lines show the evolution along individual trajectories, while the black line is the median of all trajectories at each time step and the interquartile range is shaded.

in Figure 3.16, we can only recognize few remnants of the diurnal cycle and no general trend. We see larger residual signals in cloud fraction compared to the residual shown in Figure 3.15. If we compare the variance that is left in the data, the residuals of both cloud metrics after removing the regression on all time series still have a variance of 43 % compared to the variance before the removal of large-scale influence. The residuals of the regression on fitted ensemble medians still contain 41 % of the variance in L_{mean} and 95 % of the variance in cf. Although we can capture the diurnal cycle in cf very well, the prediction still deviates a lot both positively and negatively from the true cloud fraction.

Looking back at the flow fields, we can compare the original flow field in its standardized version (Figure 3.17) with the ones resulting from the residual cloud metrics (Figure 3.18). In both of the flow fields of residual cloud metric tendencies we see a convergence towards the center, which is in both cases slightly below the mean in both cloud metrics. The center in

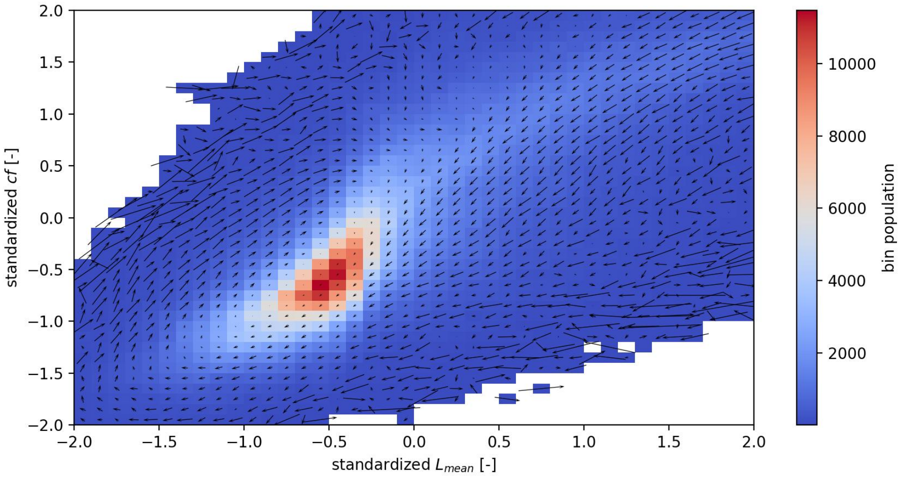

Figure 3.17: Gauss-filtered mean tendencies in cloud metric space of both standardized mean object length and cloud fraction. Standardization was done by subtracting the mean and dividing by the standard deviation. The arrows show the mean change per hour of cloud fields that are located within the corresponding bin. The tendencies were obtained for every 10 min increment along all trajectories. The background color displays the number of data points per bin.

Figure 3.18a is more widespread because the diurnal cycle is still left in the residual cloud metrics. In Figure 3.18b the center is more circular as the diurnal cycle is largely removed and the residual metrics vary in all directions in metric space. The bin population is higher for residual mean object length that are slightly smaller than the mean value, which can be caused by the positive bias of our regression seen in Figure 3.14.

Both flow fields resemble the behavior of noise, where the mean tendencies point towards the mean value in the center of the standardized space. Thus, we are not able to see a systematic mesoscale self organization after we removed the influence of the macroscale. To find this self organization, we would need to gain an even better understanding of the processes of the large scale influence in order to not remove variance that is actually unrelated to to it. On the other hand, we need to select the right cloud controlling factors, which might be at different pressure levels in reality compared to LES. For example the sub-cloud relative humidity can explain variance in cloud fraction, but it is questionable if it actually controls the clouds. The best regression does not always inform us about the true physical relations, but from our point of knowledge it is not possible to identify mesoscale self-organization from removing the large-scale influence from the mesoscale signal.

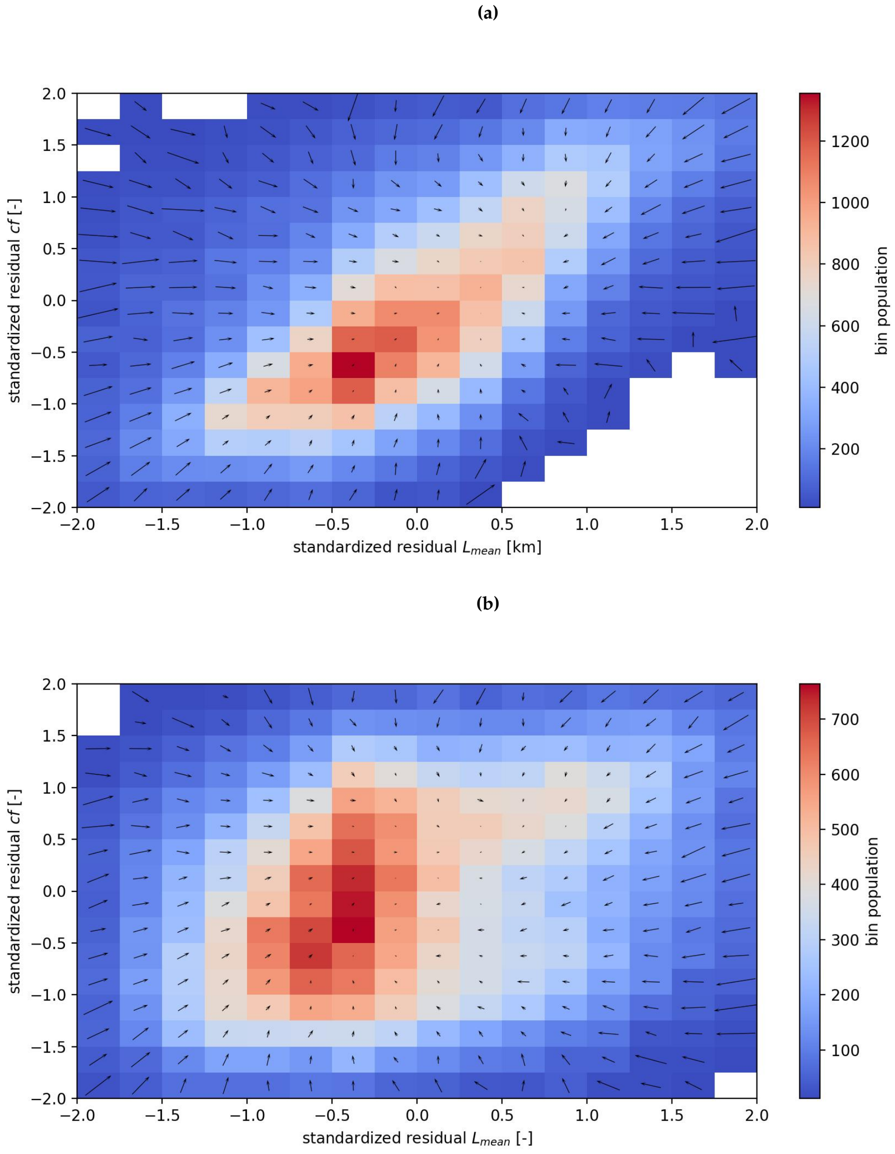

Figure 3.18: Residual mean tendencies in cloud metric space of standardized mean object length and cloud fraction after subtracting the predicted cloud metrics from a) the full data regression and b) the regression on fitted medians. The arrows show the mean change per hour of cloud fields that are located within the corresponding bin. The tendencies were obtained for every 3 local hour increment along all trajectories. The background color displays the number of data points per bin.

4

Discussion

In this section we want to discuss some of the limitations of the study and possible solutions as well as implications that we can draw from the results. It is meant to shine a critical light on the findings and their robustness and to show how it could be improved and to what cost. First, we discuss other methods to track cloud fields in a Lagrangian framework (section 4.1), then we review possibilities to identify patterns of shallow cumulus clouds. Subsequently, in section 4.3 we discuss possible ways how the large scale circulation could couple with the mesoscale. Finally, we look at implications of our results for the cloud radiative effect and discuss possible feedback mechanisms qualitatively.

4.1. Lagrangian tracking of cloud fields

Trajectories of air masses and their cloud fields obtained by reanalysis winds have been applied in multiple studies for stratocumulus, trade cumulus and the transition between the two regimes (Eastman and Wood, 2015; Sandu et al., 2010; Schulz et al., 2021). Bretherton et al. (2010) showed that the ECMWF operational analysis output of wind components below the cloud layer is consistent with real measurements. This indicates that we can trust this method at least for temporal resolutions of 12 h where it has been applied so far. The spline interpolation on hourly trajectory points and linear interpolation in between appears to have reasonable small errors if we compare it to the frame size we compute the metrics on. However, to quantify the error in the trajectories thoroughly, statistics about the drift of large cloud objects inside the Lagrangian frame would need to be performed. Therefore, the Tracking and Object-Based Analysis of Clouds (tobac) package can be used. It is identifying cloud objects based on (multiple) given thresholds of, in our case, the brightness temperature and performing a segmentation. The centroids of the cloud objects are then linked to the object in the subsequent image that is closest to the objects original position or its position predicted from previous movement, depending on the chosen method. This results in tracks of individual cloud objects. However, we find that the results of this tracking method are very sensitive to cloud objects splitting and merging and are more robust for larger cloud objects. While this makes it difficult to use tobac to obtain trajectories for a whole field of clouds and even impossible if the sky is cloud free, the tracking algorithm could be used to evaluate the statistics of cloud object drift relative to the frames along the ERA5 trajectories. This could proof that the framework of Eastman and Wood, 2015 is also applicable on shorter timescales.

Another option to track clouds from a computer science perspective is matching subsequent cloud images using the so called Earth Mover Distance (EMD) as matching cost. The method is originally developed for image retrieval (Rubner et al., 2000), but it can also be extended to detecting the movement of features, for example clouds Ji et al., 2006. If the cloud objects are considered a two-dimensional distribution the EMD is the minimal work that must be performed to translate one distribution into the other. The method is promising to be more robust than the linking algorithm of tobac that is only based on minimal search distance between the centriods of cloud features and the EMD could be minimized for a whole frame, such that we can directly obtain the resulting movement of the entire cloud field. Even so, this method has not been thoroughly tested on tracking cloud fields yet and would need to be compared to ERA5 trajectories in their ability of following cloud fields and computational efficiency.

Though these methods are interesting alternatives and could be used to test how well the clouds are following the trajectories, the method that best suits the Lagrangian approach is to follow the air masses where the clouds are moving in (as done by the ERA5 trajectories), instead of the objects themselves. Considering the vertical component would be the next step to gain more accuracy, but especially along the strong trade winds the vertical component is negligible small in comparison.

As a last note, for more robust statistics over ensembles of trajectories, the trajectories should be chosen with the same length without loosing their alignment in local time to see diurnal cycles. This was not possible in this study without reducing the amount of data to a minimum. Therefore, if the number of trajectories is increased, we can sort more rigorously for the ones that fulfill the conditions of a minimum length while staying in the studied domain and preferably not enter storm tracks.

4.2. Identification of shallow cumulus and mesoscale pattern

The shallow cumulus clouds in this thesis are simply defined by the binary cloud mask described in section 2.3, where shallow cumuli have cloud top brightness temperatures between 280–290 K. This simple method is also applied in multiple other studies (Bony, Schulz, et al., 2020,Vial, Vogel, et al., 2021) and has proven efficient in identifying the Sugar, Gravel, Fish and Flower patterns. The problem remains that higher clouds are considered as non-cloudy pixels by the cloud mask. While we do not want to include Cirrus clouds, clouds that experience deeper convection and have tops that are colder than 280 K could be considered, for example by using multiple thresholds and more levels in the cloud mask. This way more scenes with high clouds could still be considered and the metrics could be computed on the different levels as well.

Further, instead of only considering the brightness temperature one could also measure the cloud optical depth of the clouds as it is relevant for the cloud albedo and therefore the CRE. The mean object length scale used in our analysis is correlated with the cloud optical depth (Alinaghi et al., 2023; Janssens, 2023), but the direct measurement would certainly add value to the analysis.

The classification of mesoscale patterns with cloud metrics has big advantages by being objective and not limited to a subset of predefined states, but conveying the continuum of states in pattern space. One disadvantage is that the scene size needs to be constant as some of the cloud metrics are sensitive to the scene. Other methods, like the deep neural network trained on visual images by Rasp et al., 2020 and extended on brightness temperature inputs by Schulz et al., 2021, are able to identify patterns in scenes of variable size. This is especially usefull as we know that patterns can differ a lot in size, like Fish and small extents of Sugar. The neural network classification could even be used to link rectangles of patterns in subsequent images and thereby tracking cloud fields. This would, however, only be applicable as long as the patterns do not transition between the Sugar, Gravel, Fish and Flower classes. The transition states would likely not be recognized by the neural network because it is only trained on distinct classes. The training process makes the neural network as subjective as the labelling method of the training data. Therefore, a deep neural network could be trained with scenes that are characterized by cloud metrics before and sorted into classes that can still be consistently identified by the neural network, but that leave no transitional states in the metric space. This way, we could combine the advantages of both methods and objectively identify patterns of various sizes based on the visual appearance of a certain cloud metrics state and track their spatial and metric evolution. Though, this method would cost much training and testing effort and it is uncertain if it would perform better than the pure classification by cloud metrics on frames of a reasonable size. The ideal frame never contains more than one type of pattern, but is large enough to identify larger patterns that only fit partially into the frame. Based on the experience of other studies Janssens et al., 2021 and our comparison with smaller frame sizes we chose the 5°×5° frames, but a more systematic analysis can help to find the ideal frame size for a given set of cloud metrics.

4.3. Coupling between large scale and mesoscale

The question on how the different meteorological scales couple with each is other is a very central question in cloud research. Because our observations cannot resolve the microscale (GOES-16 resolution of 2 km), we constrain this discussion to the macroscale and the mesoscale. The cloud controlling factors belong to the large scale circulation and prescribe by definition the parameters that control the mesoscale to a certain extent. Our results imply that the mean state of the mesoscale can be explained by the large-scale, but there is an unexplained variance of more than 40 % left in the cloud metrics. This could be because other important CCFs are missing in our regression, like the free-tropospheric humidity or the temperature advection. Because our trajectories include the transition from stratocumulus to trade cumulus, the regression coefficients could also be dependent on the sub-regime they are in. To consider this, one could separate the regressions and perform them independently on both sub-regimes, resulting in the regression functions $f_{Sc}(\mathcal{L})$ for stratocumulus and $f_{Cu}(\mathcal{L})$ for trade cumulus that both depend on the large-scale conditions $\mathcal{L}$. The transition could then be included by a third function $t(\mathcal{L})$ that gives the respective weight of the two regressions and is dependent on large-scale variables that are known to control the transition (SST and LTS following Sandu et al., 2010). The resulting regression from large scale onto the mesoscale would then be

$$f(\mathcal{L}) = t(\mathcal{L}) \cdot f_{Cu}(\mathcal{L}) + (1 - t(\mathcal{L})) \cdot f_{Sc}(\mathcal{L}). \tag{4.1}$$

As already discussed in subsection 3.5.2 for the lower tropospheric stability, lags between the cloud controlling factors and their effect onto the cloud metrics are likely to exist. Ideally, the regressors would be weighted integrals over the history of the cloud controlling factors with a maximum weight at some lag Δt. This would make the analysis a lot more sophisticated. A simpler version would be to investigate the lags between all CCFs and the cloud metrics, for example by introducing sudden changes in the large-scale conditions in LES models and compare the resulting evolution of the cloud metrics to those in an unperturbed environment.

If we presume that the mesoscale can also develop on its own in the self-organization process, the question arises how the two forcings are coupled. Both, the mesoscale state imposed by the cloud controlling factors and the self-organization term are assumed linear and additive separable in this thesis. This simple relation is motivated by simulations that keep the large scale constant and find self-organization independent of what the chosen large-scale parameters are (Jansson et al., 2023). It is assuming a linear dynamical system, where the large-scale forcing and the mesoscale forcing are independent of each other. The residual cloud metric state therefore describes only that part of the mesoscale that is completely independent of the large scale. If we call the macroscale state $\mathcal{L}$, the observable mesoscale state $\mathcal{M}$ and the state of (in-)dependent mesoscale self organization $\mathcal{M}_s$ this translates to the equation

$$\mathcal{M} = f(\mathcal{L}) + \mathcal{M}_s, \tag{4.2}$$

where the function f contains the linear regression on CCFs. This decomposition would result in the equation of motion

$$\frac{\mathrm{d}\mathcal{M}}{\mathrm{d}t} = \frac{\mathrm{d}f(\mathcal{L})}{\mathrm{d}t} + \frac{\mathrm{d}\mathcal{M}_s}{\mathrm{d}t} = \boldsymbol{F}_{\mathcal{L}} + \boldsymbol{F}_{\mathcal{M}_s} = \boldsymbol{F}_{\mathcal{M}}, \tag{4.3}$$

where the large scale forcings $\boldsymbol{F}_{\mathcal{L}}$ can further be separated into its CCF components. In our analysis we assume the self-organizational forcing to be independent of the large scale, i.e. $\boldsymbol{F}_{\mathcal{M}_s} = \boldsymbol{F}_{\mathcal{M}_s}(\mathcal{M}_s)$. However, we do not know about the physicality of $\mathcal{M}_s$, while $\mathcal{M}$ is observable in the form of cloud metrics. Thus, one could argue that the forcing should be depending on the mesoscale state $\boldsymbol{F}_{\mathcal{M}_s} = \boldsymbol{F}_{\mathcal{M}_s}(\mathcal{M})$, making it indirectly dependent on the large scale. This could be analyzed by keeping the flow field in its original state (cf. Figure 3.8) and only change the tendencies, by removing the large-scale forcing.

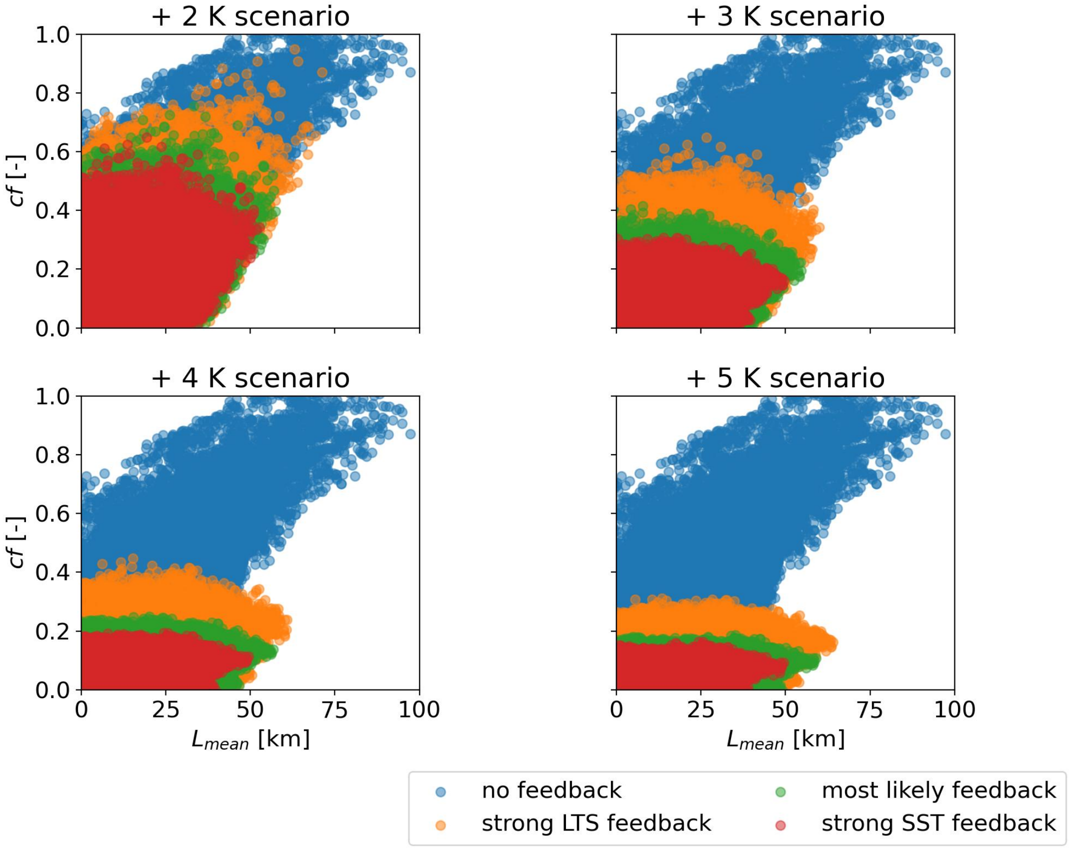

Figure 4.1: Change in cloud metrics for four scenarios of global surface temperature increase assuming the observed temperature increase of 1 K (cf. IPCC, 2021) already in equilibrium for the state of our analysis 2020 ("no feedback"). Note that SST increase can take multiple decades, such that its feedback here might be underestimated. The "strong SST feedback" case uses +2 std. dev. 1/K SST feedback and zero feedback for LTS, the "strong LTS feedback" case uses +1 std. dev. 1/K and 0.3 std. dev. 1/K for SST and LTS, respectively, and the "most likely feedback" case uses 1.6 std. dev. 1/K and 0.2 std. dev. 1/K.

4.4. Implications for cloud radiative effect

Let us finally look at the implications of our results for the cloud radiative effect (CRE). Because the cloud optical depth determines the cloud albedo and is correlated with the mean object length (Alinaghi et al., 2023) we can qualitatively discuss the change in CRE caused by a change in cloudiness predicted from our CCF regression.

We will consider the regression on the fits of ensemble median time series shown in Figure 3.13 and introduce different cloud-regime-averaged CO_2-forced changes in the relevant CCFs projected by GCMs and summarized in Myers, Scott, et al., 2021. The largest changes (in units of standard deviation of natural variability per degree global warming) are in SST and and the estimated inversion strength EIS, which is strongly correlated with LTS (Bony, Schulz, et al., 2020). Changes in SST are between 1 and 2 standard deviations per degree global warming for stratocumulus and trade cumulus, while EIS increases slightly between 0 and 0.3 standard deviations. We assume the same change in LTS, which is linear in our regression for L_{mean} and with the standardized regression coefficient of about 12 km this translates to an increase in mean object length of 0–3.6 km/K induced by LTS change. On the other hand, both mean object length and cloud fraction decrease exponentially with SST increase, such that it has a stronger effect on stratocumulus than on trade cumulus and counteracts the increase in mean length scale in both sub-regimes.

In Figure 4.1 four scenarios of global surface temperature increase are shown, each comparing

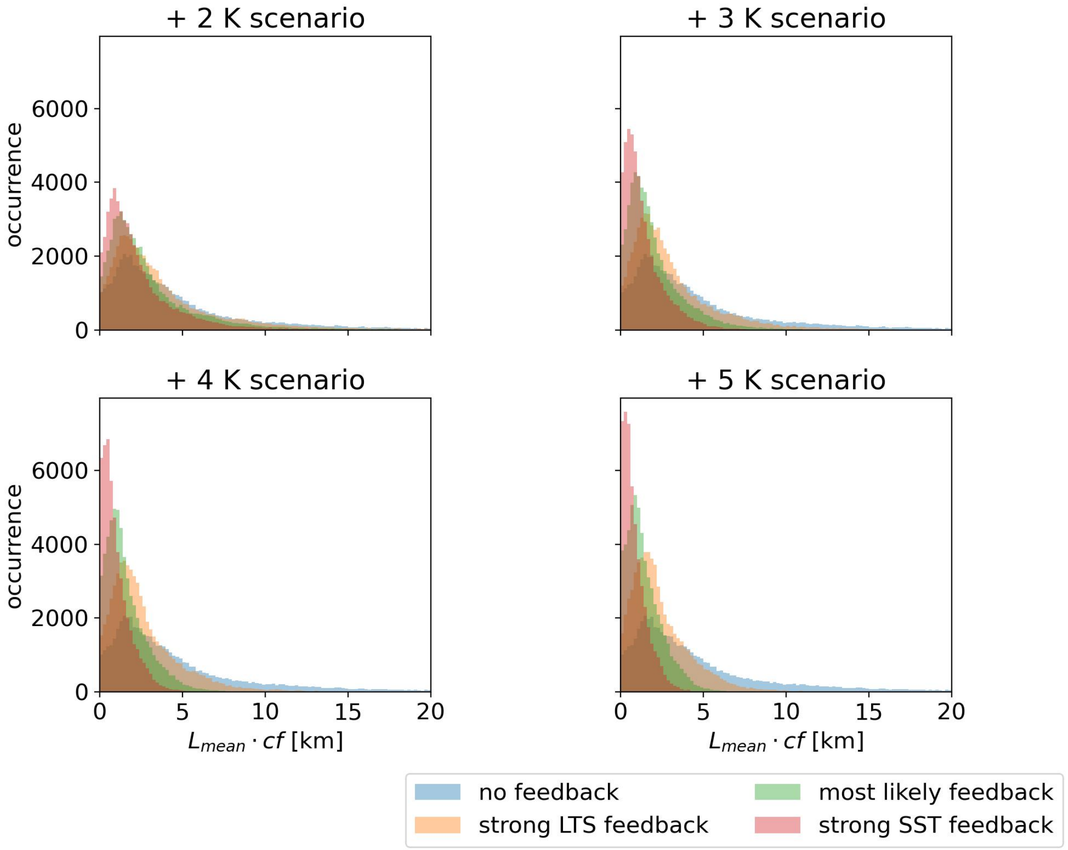

Figure 4.2: Change in distribution of $L_{\text{mean}} \cdot cf$ as an indicator of CRE for same scenarios and cases as in Figure 4.1.

the cases of a most likely feedback, a strong SST feedback and a strong LTS feedback with the 2020 case without cloud feedback. In all four climate change scenarios the changes are the strongest for a strong SST feedback and the weakest for a strong LTS feedback, while the most likely scenario is in between the two. If we compare the different scenarios for the same case, we see the mean object length being almost invariant, while the cloud fraction decreases roughly exponentially with the temperature increase. This is because the effects of SST and LTS increase compensate each other in the regression of the mean object size. Even in the strong LTS feedback case we see the very large cloud objects with high cloud fraction become less often. This is indicating less stratocumulus type of clouds and more trade cumulus clouds. The implications for the cloud radiative effect can be estimated by looking at how the product $L_{\text{mean}} \cdot cf$ changes its distribution in the different scenarios (cf. Figure 4.2). Note that this product is proportional to CRE and has no direct quantitative interpretation. We see that the distribution is shifted to smaller values in all scenarios, indicating a negative change in CRE and thus a positive cloud feedback. This effect is the strongest in the case of strong SST feedback and the weakest in the case of strong LTS feedback. In that case the peak occurrence does not even shift significantly in all four scenarios. The most likely case is in between the other two cases. We also see that the distribution changes the most between the 2 K and 3 K scenario and is hardly distinguishable between the 4 K and 5 K scenario. This is due to our assumption of an exponential decrease in both cloud metrics with increasing SST. Small changes have a large effect, but larger changes in global temperature reach a saturation. We should mention though, that it is unlikely that our regression still holds in such a different climate scenario.

Further, only two cloud controlling factors were taken into account here. Myers, Scott, et al., 2021 shows that the more cloud controlling factors are included in the projection of the cloud feedback, the more they compensate for each other and the smaller the overall feedback. Thus, including more CCFs might lead to less significant changes in the CRE. Including the feedback in windspeed in our analysis here does not change a lot as both its regression coefficient and the proposed feedback by Myers, Scott, et al., 2021 are small compared to other effects.

5

Conclusion and Outlook

We investigated the evolution of the mesoscale organization in trade cumulus clouds within a Lagrangian framework by computing time series of cloud metrics on GOES-16 images along ERA5 trajectories. The cloud metrics were computed every 10 min on 5°×5° frames and ERA5 cloud controlling factors were available every 3 h.

The mean cloud object length and the cloud fraction both show a transition from stratocumulus to trade cumulus during the first three days as some of the trajectories start in the eastern Atlantic, where stratocumulus prevail. Over the full six day length of the time series we found a diurnal cycle in both cloud metrics. The cycle of the cloud fraction is on average 2 h ahead of the cycle of the mean cloud object length, but the distance increases as the period of the object length is slightly longer than that of the cloud fraction. Both have a period longer than the expected 24 local hours, which also indicates that the processes connected to the diurnal cycle change with the transition from stratocumulus to trade cumulus.

The diurnal cycle is also a prominent feature in the evolution of cloud fields in cloud metrics space. Actual stable states were not found, but an almost cloud-free sky with few small clouds lasts the longest. Once the mean cloud objects become small after the transition from stratocumulus only very few grow to larger mean objects lengths than 30 km again. Most cloud fields remain in a limit cycle that shifts to smaller cloud sizes and cloud fractions. In the diurnal cycle during the night small clouds form before they grow to larger objects. During the day the clouds evaporate again until only few small clouds remain.

From the decorrelation times we can conclude that the cloud fraction has a slightly longer memory than the mean cloud object length, but both of them change roughly on the same timescales as the cloud controlling factors that exhibit a diurnal cycle. The sea-surface temperature which does not show diurnality in our time series has a decorrelation time twice as long compared to the cloud metrics. In order to separate the timescales of cloud controlling factors and cloud metrics we would need the decorrelation times to be significantly longer for all cloud controlling factors. The cloud metrics, that we use to quantify the mesoscale organization, change almost simultaneously with the large scale. Thus, in contrast to simulations, the evolution of the mesoscale in an approximately constant environment is very difficult to observe.

Assuming a linear coupling between the large-scale forcing and the forcing of the mesoscale self-organization, we regressed the large-scale influence to remove it from our timeseries and obtain only the mesoscale forcing. We conclude that the sea-surface temperature is controlling the stratocumulus-cumulus-transition, while the lower tropospheric stability most likely controls the diurnal cycle in mean cloud object length and the surface wind speed is positively correlated with the cloud fraction. The role of the surface relative humidity remains unclear as it likely only co-evolves with the cloud fraction. Future studies should include the free tropospheric relative humidity to see if it can better explain the diurnality in cloud fraction together with the surface wind speed.

The variability in cloud metrics explained by cloud controlling factors is larger than 50 % if

the regression is performed on the individual time series. This value increases if we compute temporally averages that remove the diurnal cycle in the time series. By only using the analytical fits on the ensemble median time series of cloud controlling factors and metrics in the regression, the explained variability increased to almost 100 %
Still, after removing the large-scale forcing more than 40 % of the variance in the cloud metrics remained. This indicates that more processes, possibly on the mesoscale, play a role in controlling the cloudiness, if the remaining variance is not solely due to random noise. However, from the analysis of the residual signal in the cloud metrics, we can only derive that the cloud fields are forced into the mean state that is explained by the large scale, a result we expect from random noise. Based on our regressions we can estimate that the low cloud feedback is positive and stronger for stratocumulus than for trade cumulus.
The question, whether processes on the mesoscale can lead to organization independent of the large-scale, as shown in simulations, can not be finally answered. As our goal is to predict the cloudiness in the trades for warmer climates, the large remaining variance in the mesoscale should be further investigated. The timescales for observing the mesoscale evolving independently from the large-scale are very short and presumably not captured by the 3 h averaged data we used. Therefore, following studies should interpolate the cloud controlling factors onto shorter timescales or even use data with a higher temporal resolution, like hourly ERA5 variables. Further, the dataset should be expanded in the number of trajectories and spread over multiple winter seasons. This way, not only the statistics can become more robust, but also the interannual variability can be investigated, leading to better climate feedback projections. Finally, the processes that control the stratocumulus-cumulus-transition can be studied closer, now that Lagrangian analyses with high temporal resolution are possible. A separate study should exclusively focus on the trade cumulus regime, such that the gained knowledge of both can contribute to a full picture of the low subtropical marine cloudiness. Based on these observations climate models could be better constrained and the intermodel spread could be reduced, which would result in a more accurate estimate of the climate sensitivity of our planet.

References

Albright, Anna Lea, Bjorn Stevens, Sandrine Bony, and Raphaela Vogel (2023). "A New Conceptual Picture of the Trade Wind Transition Layer". In: *Journal of the Atmospheric Sciences* 80.6, pp. 1547–1563. doi: `10.1175/jas-d-22-0184.1`.

Alinaghi, Pouriya, Martin Janssens, Goutam Choudhury, Tom Goren, A Pier Siebesma, and Franziska Glassmeier (2023). "Shallow Cumulus Cloud Fields Are Optically Thicker When They Are More Clustered". In: *arXiv preprint arXiv:2309.08346*.

Bony, Sandrine (2005). "Marine boundary layer clouds at the heart of tropical cloud feedback uncertainties in climate models". In: *Geophysical Research Letters* 32.20. doi: `10.1029/2005gl023851`.

Bony, Sandrine, Hauke Schulz, Jessica Vial, and Bjorn Stevens (2020). "Sugar, Gravel, Fish, and Flowers: Dependence of Mesoscale Patterns of Trade-Wind Clouds on Environmental Conditions". In: *Geophysical Research Letters* 47.7. doi: `10.1029/2019gl085988`.

Bony, Sandrine, Bjorn Stevens, Felix Ament, Sebastien Bigorre, Patrick Chazette, Susanne Crewell, Julien Delanoë, Kerry Emanuel, David Farrell, Cyrille Flamant, Silke Gross, Lutz Hirsch, Johannes Karstensen, Bernhard Mayer, Louise Nuijens, James H. Ruppert, Irina Sandu, Pier Siebesma, Sabrina Speich, Frédéric Szczap, Julien Totems, Raphaela Vogel, Manfred Wendisch, and Martin Wirth (2017). "EUREC4A: A Field Campaign to Elucidate the Couplings Between Clouds, Convection and Circulation". In: *Surveys in Geophysics* 38.6, pp. 1529–1568. doi: `10.1007/s10712-017-9428-0`.

Bretherton, C. S., R. Wood, R. C. George, D. Leon, G. Allen, and X. Zheng (2010). "Southeast Pacific stratocumulus clouds, precipitation and boundary layer structure sampled along 20° S during VOCALS-REx". In: *Atmospheric Chemistry and Physics* 10.21, pp. 10639–10654. doi: `10.5194/acp-10-10639-2010`.

Bretherton, Christopher S. (2015). "Insights into low-latitude cloud feedbacks from high-resolution models". In: *Philosophical Transactions of the Royal Society A: Mathematical, Physical and Engineering Sciences* 373.2054, p. 20140415. doi: `10.1098/rsta.2014.0415`.

Cesana, Grégory, Anthony D. Del Genio, Andrew S. Ackerman, Maxwell Kelley, Gregory Elsaesser, Ann M. Fridlind, Ye Cheng, and Mao-Sung Yao (2019). "Evaluating models' response of tropical low clouds to SST forcings using CALIPSO observations". In: *Atmospheric Chemistry and Physics* 19.5, pp. 2813–2832. doi: `10.5194/acp-19-2813-2019`.

Denby, L. (2020). "Discovering the Importance of Mesoscale Cloud Organization Through Unsupervised Classification". In: *Geophysical Research Letters* 47.1. doi: `10.1029/2019gl085190`.

Eastman, Ryan, Isabel L. McCoy, and Robert Wood (2022). "Wind, Rain, and the Closed to Open Cell Transition in Subtropical Marine Stratocumulus". In: *Journal of Geophysical Research: Atmospheres* 127.20. doi: `10.1029/2022jd036795`.

Eastman, Ryan and Robert Wood (2015). "Factors Controlling Low-Cloud Evolution over the Eastern Subtropical Oceans: A Lagrangian Perspective Using the A-Train Satellites". In: *Journal of the Atmospheric Sciences* 73.1, pp. 331–351. doi: `10.1175/jas-d-15-0193.1`.

Forster, P., T. Storelvmo, K. Armour, W. Collins, J.-L. Dufresne, D. Frame, D.J. Lunt, T. Mauritsen, M.D. Palmer, M. Watanabe, M. Wild, and H. Zhang (2021). "The Earth's Energy Budget, Climate Feedbacks and Climate Sensitivity". In: *Climate Change 2021 – The Physical Science Basis: Working Group I Contribution to the Sixth Assessment Report of the Intergovernmental Panel on Climate Change*. Cambridge University Press, pp. 923–1054.

Gettelman, A. and S. C. Sherwood (2016). "Processes Responsible for Cloud Feedback". In: *Current Climate Change Reports* 2.4, pp. 179–189. doi: `10.1007/s40641-016-0052-8`.

Hartmann, Dennis L., Maureen E. Ockert-Bell, and Marc L. Michelsen (1992). "The Effect of Cloud Type on Earth's Energy Balance: Global Analysis". In: *Journal of Climate* 5.11, pp. 1281–1304. DOI: `10.1175/1520-0442(1992)005<1281:teocto>2.0.co;2`.

Hersbach, Hans, Bill Bell, Paul Berrisford, Shoji Hirahara, András Horányi, Joaquín Muñoz-Sabater, Julien Nicolas, Carole Peubey, Raluca Radu, Dinand Schepers, Adrian Simmons, Cornel Soci, Saleh Abdalla, Xavier Abellan, Gianpaolo Balsamo, Peter Bechtold, Gionata Biavati, Jean Bidlot, Massimo Bonavita, Giovanna De Chiara, Per Dahlgren, Dick Dee, Michail Diamantakis, Rossana Dragani, Johannes Flemming, Richard Forbes, Manuel Fuentes, Alan Geer, Leo Haimberger, Sean Healy, Robin J. Hogan, Elías Hólm, Marta Janisková, Sarah Keeley, Patrick Laloyaux, Philippe Lopez, Cristina Lupu, Gabor Radnoti, Patricia de Rosnay, Iryna Rozum, Freja Vamborg, Sebastien Villaume, and Jean-Noël Thépaut (2020). "The ERA5 global reanalysis". In: *Quarterly Journal of the Royal Meteorological Society* 146.730, pp. 1999–2049. DOI: `10.1002/qj.3803`.

IPCC (2021). "Summary for Policymakers". In: *Climate Change 2021 – The Physical Science Basis: Working Group I Contribution to the Sixth Assessment Report of the Intergovernmental Panel on Climate Change*. Cambridge University Press, pp. 3–32.

Janssens, Martin (2023). "Mesoscale cloud patterns in the trade-wind boundary layer". PhD thesis. DOI: `10.18174/635857`.

Janssens, Martin, Jordi Vilà-Guerau de Arellano, Marten Scheffer, Coco Antonissen, A. Pier Siebesma, and Franziska Glassmeier (2021). "Cloud Patterns in the Trades Have Four Interpretable Dimensions". In: *Geophysical Research Letters* 48.5. DOI: `10.1029/2020gl091001`.

Jansson, Fredrik, Martin Janssens, Johanna H. Grönqvist, A. Pier Siebesma, Franziska Glassmeier, Jisk Attema, Victor Azizi, Masaki Satoh, Yousuke Sato, Hauke Schulz, and Tobias Kölling (2023). "Cloud Botany: Shallow Cumulus Clouds in an Ensemble of Idealized Large-Domain Large-Eddy Simulations of the Trades". In: *Journal of Advances in Modeling Earth Systems* 15.11. DOI: `10.1029/2023ms003796`.

Ji, Guangfeng and Han-Wei Shen (2006). "Feature tracking using earth mover's distance and global optimization". In: *Pacific graphics*. Vol. 2. Citeseer Princeton, NJ, USA.

Klein, Stephen A., Alex Hall, Joel R. Norris, and Robert Pincus (2017). "Low-Cloud Feedbacks from Cloud-Controlling Factors: A Review". In: *Surveys in Geophysics* 38.6, pp. 1307–1329. DOI: `10.1007/s10712-017-9433-3`.

Konsta, Dimitra, Jean-Louis Dufresne, Hélène Chepfer, Jessica Vial, Tsuyoshi Koshiro, Hideaki Kawai, Alejandro Bodas-Salcedo, Romain Roehrig, Masahiro Watanabe, and Tomoo Ogura (2022). "Low-Level Marine Tropical Clouds in Six CMIP6 Models Are Too Few, Too Bright but Also Too Compact and Too Homogeneous". In: *Geophysical Research Letters* 49.11. DOI: `10.1029/2021gl097593`.

Krueger, Arthur F. and Sigmund Fritz (1961). "Cellular Cloud Patterns revealed by Tiros I". In: *Tellus* 13.1, pp. 1–7. DOI: `10.3402/tellusa.v13i1.9440`.

McCoy, Daniel T., Ryan Eastman, Dennis L. Hartmann, and Robert Wood (2017). "The Change in Low Cloud Cover in a Warmed Climate Inferred from AIRS, MODIS, and ERA-Interim". In: *Journal of Climate* 30.10, pp. 3609–3620. DOI: `10.1175/jcli-d-15-0734.1`.

Medeiros, Brian and Louise Nuijens (2016). "Clouds at Barbados are representative of clouds across the trade wind regions in observations and climate models". In: *Proceedings of the National Academy of Sciences* 113.22. DOI: `10.1073/pnas.1521494113`.

Medeiros, Brian and Bjorn Stevens (2009). "Revealing differences in GCM representations of low clouds". In: *Climate Dynamics* 36.1–2, pp. 385–399. DOI: `10.1007/s00382-009-0694-5`.

Myers, Timothy A. and Joel R. Norris (2016). "Reducing the uncertainty in subtropical cloud feedback". In: *Geophysical Research Letters* 43.5, pp. 2144–2148. DOI: `10.1002/2015gl067416`.

Myers, Timothy A., Ryan C. Scott, Mark D. Zelinka, Stephen A. Klein, Joel R. Norris, and Peter M. Caldwell (2021). "Observational constraints on low cloud feedback reduce uncertainty of climate sensitivity". In: *Nature Climate Change* 11.6, pp. 501–507. DOI: `10.1038/s41558-021-01039-0`.

Nuijens, Louise and A. Pier Siebesma (2019). “Boundary Layer Clouds and Convection over Subtropical Oceans in our Current and in a Warmer Climate”. In: *Current Climate Change Reports* 5.2, pp. 80–94. DOI: `10.1007/s40641-019-00126-x`.

Qu, Xin, Alex Hall, Stephen A. Klein, and Anthony M. DeAngelis (2015). “Positive tropical marine low-cloud cover feedback inferred from cloud-controlling factors”. In: *Geophysical Research Letters* 42.18, pp. 7767–7775. DOI: `10.1002/2015gl065627`.

Radtke, Jule, Thorsten Mauritsen, and Cathy Hohenegger (2021). “Shallow cumulus cloud feedback in large eddy simulations – bridging the gap to storm-resolving models”. In: *Atmospheric Chemistry and Physics* 21.5, pp. 3275–3288. DOI: `10.5194/acp-21-3275-2021`.

Rasp, Stephan, Hauke Schulz, Sandrine Bony, and Bjorn Stevens (2020). “Combining Crowd-sourcing and Deep Learning to Explore the Mesoscale Organization of Shallow Convection”. In: *Bulletin of the American Meteorological Society* 101.11, E1980–E1995. DOI: `10.1175/bams-d-19-0324.1`.

Rubner, Yossi, Carlo Tomasi, and Leonidas J Guibas (2000). “The earth mover’s distance as a metric for image retrieval”. In: *International journal of computer vision* 40, pp. 99–121.

Sandu, I., B. Stevens, and R. Pincus (2010). “On the transitions in marine boundary layer cloudiness”. In: *Atmospheric Chemistry and Physics* 10.5, pp. 2377–2391. DOI: `10.5194/acp-10-2377-2010`.

Schulz, Hauke, Ryan Eastman, and Bjorn Stevens (2021). “Characterization and Evolution of Organized Shallow Convection in the Downstream North Atlantic Trades”. In: *Journal of Geophysical Research: Atmospheres* 126.17. DOI: `10.1029/2021jd034575`.

Scott, Ryan C., Timothy A. Myers, Joel R. Norris, Mark D. Zelinka, Stephen A. Klein, Moguo Sun, and David R. Doelling (2020). “Observed Sensitivity of Low-Cloud Radiative Effects to Meteorological Perturbations over the Global Oceans”. In: *Journal of Climate* 33.18, pp. 7717–7734. DOI: `10.1175/jcli-d-19-1028.1`.

Sherwood, S. C., M. J. Webb, J. D. Annan, K. C. Armour, P. M. Forster, J. C. Hargreaves, G. Hegerl, S. A. Klein, K. D. Marvel, E. J. Rohling, M. Watanabe, T. Andrews, P. Braconnot, C. S. Bretherton, G. L. Foster, Z. Hausfather, A. S. von der Heydt, R. Knutti, T. Mauritsen, J. R. Norris, C. Proistosescu, M. Rugenstein, G. A. Schmidt, K. B. Tokarska, and M. D. Zelinka (2020). “An Assessment of Earth’s Climate Sensitivity Using Multiple Lines of Evidence”. In: *Reviews of Geophysics* 58.4. DOI: `10.1029/2019rg000678`.

Stevens, B. and Sandrine Bony (2013). “What Are Climate Models Missing?” In: *Science* 340.6136, pp. 1053–1054. DOI: `10.1126/science.1237554`.

Stevens, Bjorn, Sandrine Bony, Hélène Brogniez, Laureline Hentgen, Cathy Hohenegger, Christoph Kiemle, Tristan S. L’Ecuyer, Ann Kristin Naumann, Hauke Schulz, Pier A. Siebesma, Jessica Vial, Dave M. Winker, and Paquita Zuidema (2019). “Sugar, gravel, fish and flowers: Mesoscale cloud patterns in the trade winds”. In: *Quarterly Journal of the Royal Meteorological Society* 146.726, pp. 141–152. DOI: `10.1002/qj.3662`.

Tobin, Isabelle, Sandrine Bony, and Remy Roca (2012). “Observational Evidence for Relationships between the Degree of Aggregation of Deep Convection, Water Vapor, Surface Fluxes, and Radiation”. In: *Journal of Climate* 25.20, pp. 6885–6904. DOI: `10.1175/jcli-d-11-00258.1`.

Vial, Jessica, Jean-Louis Dufresne, and Sandrine Bony (2013). “On the interpretation of inter-model spread in CMIP5 climate sensitivity estimates”. In: *Climate Dynamics* 41.11-12, pp. 3339–3362. DOI: `10.1007/s00382-013-1725-9`.

Vial, Jessica, Raphaela Vogel, and Hauke Schulz (2021). “On the daily cycle of mesoscale cloud organization in the winter trades”. In: *Quarterly Journal of the Royal Meteorological Society* 147.738, pp. 2850–2873. DOI: `10.1002/qj.4103`.

A

Appendix

A.1. List of computed metrics

Out of the 21 cloud metrics used by Janssens et al., 2021 the following ones were computed along the trajectories:

- Maximum object length scale (L_{max})
- Mean object length scale (L_{mean})
- Cloud fraction (cf)
- Number of objects (N_{objects})
- Mean object perimeter
- Open sky (os)
- Orientation
- Fractal dimension
- I_{org}
- $SCAI$
- COP

A.2. Additional figures

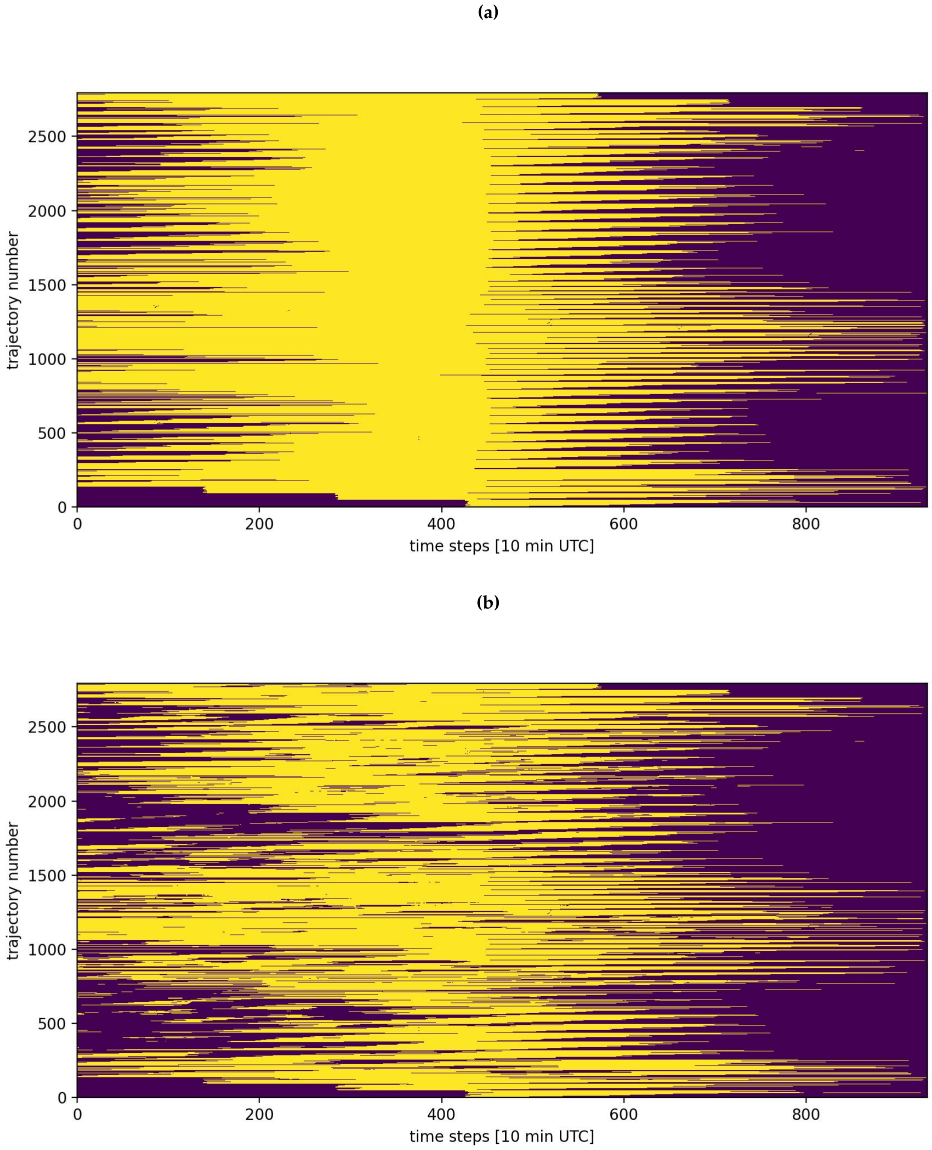
(a)

(b)

Figure A.2.1: a) Alignment of the trajectories after dropping time steps outside of the domain of observation as shown in Figure 2.1. On the x-axis the trajectory time steps are shown up to 933, which corresponds to 6.3 d in local time, and on the y-axis we see the trajectory numbers up to 2794. In yellow are time steps, where cloud metrics are computed, and in dark, where no data is available. In b) the time steps with high cloud fraction above 25 % are dropped as well. Note that for the ensemble medians the amount of trajectories that are taken into account changes over the time steps.

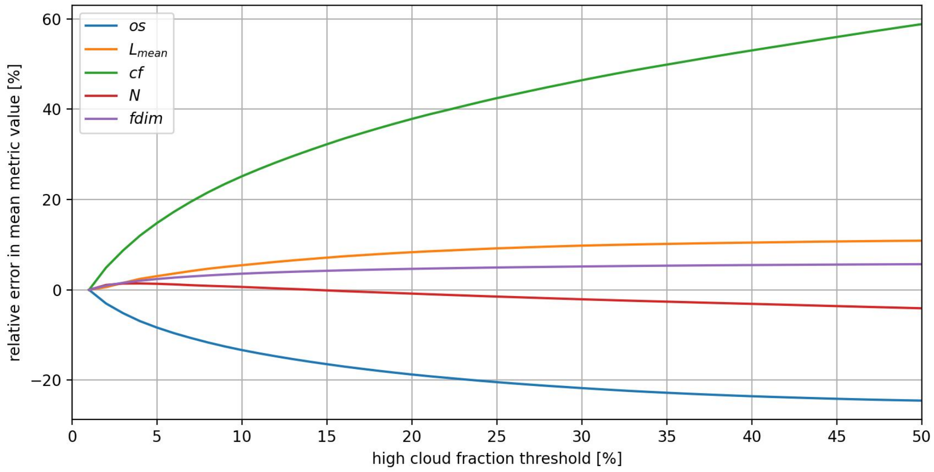

Figure A.2.2: Relative difference in mean metric values for different chosen high cloud fractions to scenes almost free of high clouds. We took the mean metric value up to the given high cloud fraction and took the ratio with the mean metric value for a high cloud fraction of less than 1 %, considered as the "undisturbed" mean. The relative difference is then shown in percent as well.

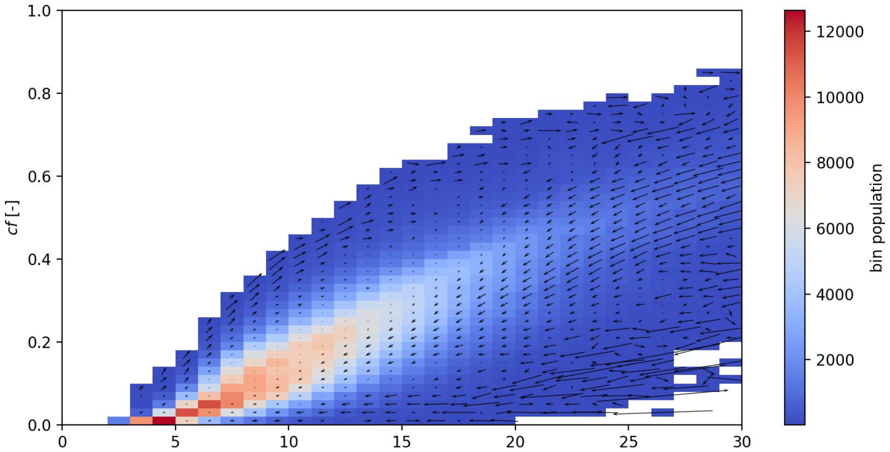

Figure A.2.3: Gauss-filtered mean tendencies in cloud metric space of mean object length and cloud fraction. The arrows show the mean change per hour of cloud fields that are located within the corresponding bin. The tendencies were obtained for every 10 min increment along all trajectories. The background color displays the number of data points per bin. The Gauss-filter was implemented with a width of $\sigma = 30$ min under the assumption that this averages out changes in the microscale and noise in the metrics, while keeping the meso- and large scale evolution unchanged.

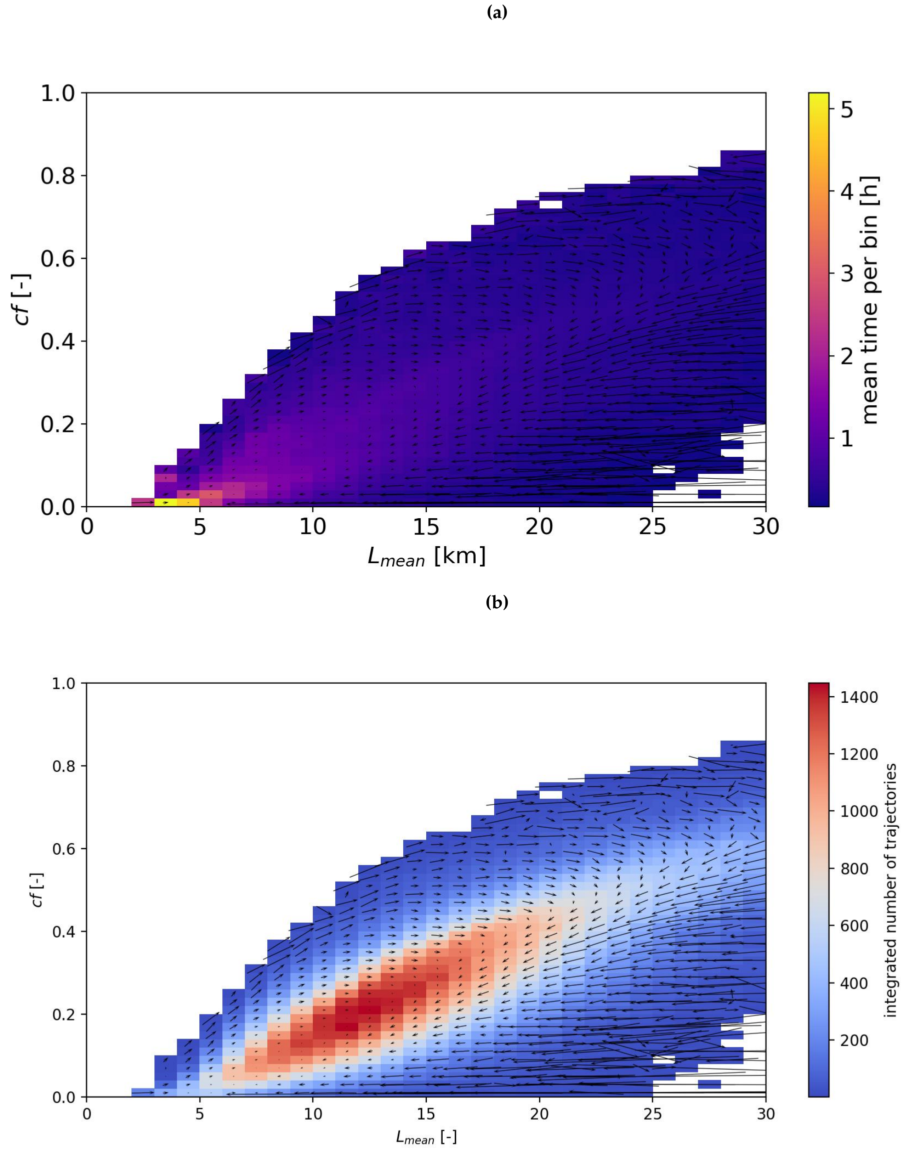

Figure A.2.4: Same as Figure 3.8 but colors indicate mean time that cloud fields spend in the corresponding bin (a), and number of trajectories that pass through the bin (b).

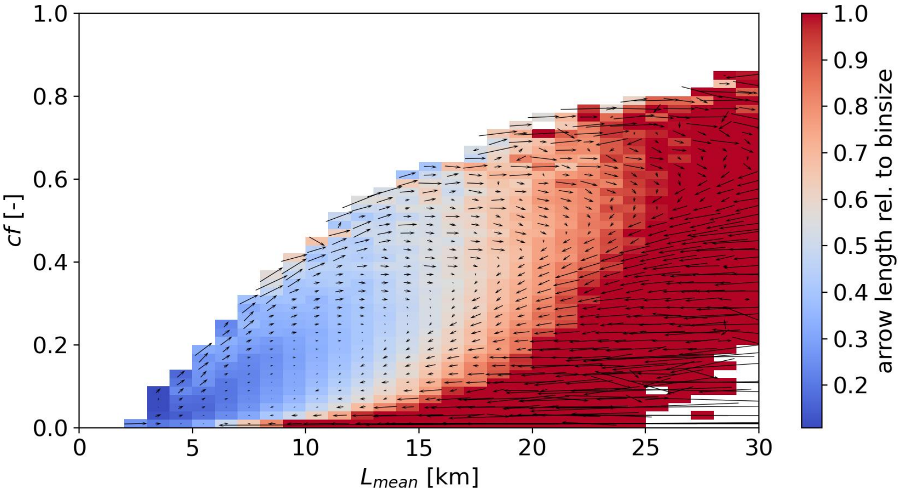

Figure A.2.5: Same as Figure 3.8 but colors indicate mean length of the arrows in each bin relative to the bin size.